UNIVERSITY OF CALIFORNIA
RIVERSIDE

Anisotropic Thermal Properties of Nanostructured Magnetic, Carbon and Hybrid Magnetic – Carbon Materials

A Dissertation submitted in partial satisfaction
of the requirements for the degree of

Doctor of Philosophy

in

Materials Science and Engineering

by

Sylvester Ramirez

March 2016

Dissertation Committee:

Prof. Alexander A. Balandin, Chairperson
Prof. Alexander Khitun
Prof. Javier Garay

The Dissertation of Sylvester Ramirez is approved by:

_____

_____

_____

Committee Chairperson

University of California, Riverside

Acknowledgements

First and foremost, I would also like to thank my former and current colleagues at the Nano-Device Laboratory (NDL) and Phonon Optimized Engineered Materials (POEM) Center. Their knowledge, experience, and cooperation aided me in succeeding and taught me much. I express my sincere gratitude to Chenglong, Mohamed, Rameez, Ruben, Sascha, Edberg, Regina, Dineth, Edward, Robert, Stanislav, Dr. Guanxiong Liu, Dr. Richard Gulotty, Dr. Denis Nika. I am especially grateful to Dr. Pradyumna Goli for his leadership and mentorship during my difficult first years. I am grateful to Dr. Jackie Renteria for her collaboration on my dissertation research involving reduced graphene oxide films. A significant part of the material in Chapter 5 was taken from our join publication J. Renteria *et al.*, *Advanced Functional Materials* 25, 4664 (2015) with permission from the publisher, John Wiley and Sons. I am grateful for their assistance and for creating a positive environment for me to work in and for their cooperation with my research.

I would also like to thank Dr. Javier Garay, Aleksey Volodchenkov, and Kyle Chan at the Advanced Materials Processing and Synthesis Laboratory. I thank Dr. Garay for his patience and for motivating me to continue my research and to succeed. I thank Aleksey for his cooperation and patience for all of his work involved in my dissertation. The results of our joint work are described in detail in Chapter 3. I also thank Kyle for his willingness to cooperate with me and pursue an idea with uncertain success at the start. Results for this work are detailed in Chapter 3.

Lastly, I express my deepest and sincerest gratitude to my family, especially my wife, for their love, patience, and support during my graduate studies. I appreciate the motivation and inspiration they supplied me and for their understanding. I am forever grateful to them.

To my wife,

Joanne

ABSTRACT OF THE DISSERTATION

Anisotropic Thermal Properties of Nanostructured Magnetic, Carbon and Hybrid Magnetic – Carbon Materials

by

Sylvester Ramirez

Doctor of Philosophy, Graduate Program in Materials Science and Engineering
University of California, Riverside, March 2016
Dr. Alexander A. Balandin, Chairperson

In this dissertation research we investigated thermal properties of three groups of nanostructured materials: (i) magnetic; (ii) reduced graphene oxide films; and (iii) hybrid magnetic – graphite – graphene composites. The thermal measurements were conducted using the transient "hot disk" and "laser flash" techniques. The rare-earth free nanostructured $SrFe_{12}O_{19}$ permanent magnets were produced by the current activated pressure assisted densification technique. The thermal conductivity of the nanostructured bulk magnets was found to range from 3.8 to 5.6 W/mK for the in-plane and 2.36 W/mk to 2.65 W/mK for the cross-plane directions, respectively. The heat conduction was dominated by phonons near the room temperature. The anisotropy of heat conduction was explained by the brick-like alignment of crystalline grains with the longer grain size in-plane direction. The thermal conductivity scales up with the average grain size and mass density of the material revealing weak temperature dependence. Using the nanostructured ferromagnetic Fe_3O_4 composites as an example system, we incorporated graphene and graphite fillers into magnetic material without changing their morphology. It was demonstrated that addition of 5 wt. % of equal mixture of graphene and graphite fillers to

the composite results in a factor of ×2.6 enhancement of the thermal conductivity without significant degradation of the saturation magnetization. We investigated thermal conductivity of free-standing reduced graphene oxide films subjected to a high-temperature treatment of up to 1000°C. It was found that the high-temperature annealing dramatically increased the in-plane thermal conductivity, K, of the films from ~3 W/mK to ~61 W/mK at room temperature. The cross-plane thermal conductivity, $K_{\perp}$, revealed an interesting opposite trend of decreasing to a very small value of ~0.09 W/mK in the reduced graphene oxide films annealed at 1000^{o}C. The obtained films demonstrated an exceptionally strong anisotropy of the thermal conductivity, $K/K_{\perp} \sim 675$, which is substantially larger even than in the high-quality graphite. The strongly anisotropic heat conduction properties of these films can be useful for the thermal filler applications. The results obtained for the nanostructured magnetic and hybrid materials are important for the renewable energy and electronic applications of permanent magnets.

Contents

List of Figures

List of Tables

Chapter 1

Introduction

Magnets are heavily used in a wide array of electronic applications. Magnets are classified in one of two categories: soft magnets and permanent magnets. Soft magnets are magnets that are easily demagnetized and do not produce a constant magnetic field when an external magnetic field is removed. Permanent magnets (PM) are magnets that are not easily demagnetized and produce a constant magnetic field even when the external magnetic field is removed. This dissertation will mainly focus on PMs as currently these materials are of great interest in clean energy generation.

1.1 Motivations

Permanent Magnets are on the rise as they are used more widely in clean energy generation (i.e. wind turbines) and electric vehicles (i.e. hybrids) [1, 2, 4]. As a result, demand for high energy product PMs is also increasing [1-2, 4]. PMs with high energy products are typically those that contain a rare-earth (RE) element, such as Neodymium (Nd) or Dysprosium (Dy), and are moderately abundant in the earth's crust and among the most critical for short term clean energy technologies [2-3]. Unfortunately, the supply of RE elements is not keeping up with the demand for RE elements [1, 3-4]. This is because the majority of RE element mines and production (approximately 97%) is in China, with no ore mines or production currently in Europe [1-2, 4]. This has led to a shortage in RE

PMs which has led to a sharp increase in price. With the increasing prevalence of electric and hybrid vehicles and the popularity of clean energy generation, RE PMs will be in even greater need in the future.

Due to the heavy increase in price in RE PMs resulting from the shortage, many alternatives to RE PMs with similar high energy product are needed. Thus, there a great push to improve the energy product of PMs that are rare-earth free (REF), or rare-earth free permanent magnets [1]. Some of the most abundant and low cost substitutions are the PMs known as the Ferrites. REF ferrites are low cost due to the Earth's abundance of Iron. However, the downside to ferrites is that they are not magnetically powerful enough to substitute RE PMs [1]. Therefore, some research is dedicating into improving ferrites' energy product [2]. The findings in this dissertation are focused on this group of REF PMs.

While most of the research is focused on the magnetic properties of PMs, there is another area of PM applications, largely ignored, that should also be improved: thermal transport and heat dissipation. The reason for this is because many of these materials are used in applications in either extreme environments or where self-heating can cause problems or both, where Samarium Cobalt PMs reign [1-2]. It is well known that magnetic materials' properties degrade at elevated temperatures which will result in an applications malfunction or reduced efficiency. Unfortunately, the thermal properties of many PMs are not known. Very few PMs, that were studied, have desirable thermal properties [3].

1.2 Dissertation Research Summary

In this dissertation, we conducted a study of the thermal properties of $SrFe_{12}O_{19}$, a REF PM whose thermal properties have not been solidified prior to this study (Chapter 3). If REF PMs are to substitute RE PMs, their thermal properties must also be matched or improved upon, or else self-heating could seriously limit their potential application. We also proposed (Chapter 4) a model system for improvement of thermal management of PMs by using graphite and graphene as filler materials for facilitating the magnet's ability to dissipate unwanted heat without seriously degrading magnetic properties (i.e. saturation magnetization) by engineering phonons. Lastly, we conducted (Chapter 5) the study of reduced graphene oxide (rGO), a material I propose to be used as a filler material for improving heat conduction in the manner described in Chapter 4. Carbon materials were selected for these experiments owing to extremely high thermal conductivity of graphene and the rising trend of creating graphite – graphene based composites [5-8].

1.3 Summary

The motivations for the research in this dissertation were discussed. Increasing demand for RE PMs and their lack of increasing supply are motivations for investigation for

alternatives to PMs. Results for thermal transport studies for $SrFe_{12}O_{19}$ are demonstrated along with thermal studies for carbon based filler composites and rGO.

References

[1] R. L. Moss, E. Tzimas, H. Kara, P. Willis and J. Kooroshy, "*Critical Metals in Strategic Energy Technologies*," *JRC Sci. and Tech. Rep*., European Union (2011)

[2] D. Bauer, D. Diamond, J. Li, M. McKittrick, D. Sandalow and P. Telleen, "*Critical Materials Strategy*," Dept. of Energy Office of Pol. & Intern. Affairs (2011)

[3] M. Humphries, "*Rare Earth Elements: The Global Supply Chain*," *Congressional Research Service*, The Lib. of Congr., Washington (2013)

[4] E. Alonso, A. M. Sherman, T. J. Wallington, M. P. Everson, F. R. Field, R. Roth and R. E. Kirchain, "*Evaluating Rare Earth Element Availability: A Case with Revolutionary Demand from Clean Technologies*," Environ. Sci. & Technol. **46**, 3406 (2012)

[5] E. Flahaut, A. Peigney, Ch. Laurent, Ch. Marliere, F. Chastel and A. Rousset, "*Carbon Nanotube–Metal–Oxide Nanocomposites: Microstructure, Electrical Conductivity And Mechanical Properties*," Acta mater. **48**, 3803 (2000)

[6] V. Goyal and A. A. Balandin, "*Thermal Properties of the Hybrid Graphene-Metal Nano-Micro-Composites: Applications in Thermal Interface Materials*," Appl. Phys. Lett. **100**, 073113 (2012)

[7] Z. Wua, G. Zhoua, L. Yina, W. Rena, F. Lia and H. Cheng, "*Graphene/metal oxide composite electrode materials for energy storage*," Nano Energy **1**, 107 (2012)

[8] J. Zhang, Z. Xiong and X. S. Zhao, "*Graphene–metal–oxide composites for the degradation of dyes under visible light irradiation*," J. Mater. Chem. **21**, 3634 (2011)

Chapter 2

Experimental Approach and Characterization Tools

In order to separate the electron, phonon, and magnon contributions to thermal conductivity, one must conduct thermal and electrical measurements. The electron contribution can be approximately obtained using the Wiedemann-Franz law by relating the electrical conductivity to its thermal conductivity. The phonon contribution can be determined as a difference between the total thermal conductivity and electronic thermal conductivity. The magnon contribution in magnetic materials, if necessary, can be obtained through a similar setup as with phonon measurements with the addition of an external magnetic field to observe the changes in thermal conductivity, if any.

2.1 Laser Flash Method

Sample preparation is important for laser flash measurements. Density and mass must be measured prior to measurements because they are needed for extraction of the thermal diffusivity and conductivity. After density and mass are measured, the sample must be coated lightly with graphite. This coat will help with transmittance when exposed to the

flash lamp so that the sample absorbs as much heat as possible. However, too much coating can affect diffusivity and conductivity results. After preparation, the sample is ready for measurements.

Laser flash is a transient method for measuring the thermal conductivity of materials, different from other steady-state methods like the 3ω technique. Laser flash method uses an optical source to heat the sample under observation and relies on the sample material data, such as specific heat and density, to calculate thermal diffusivity. The instrument used for these experiments in this dissertation research is the LFA 447 by Netzsch with Nano Flash software.

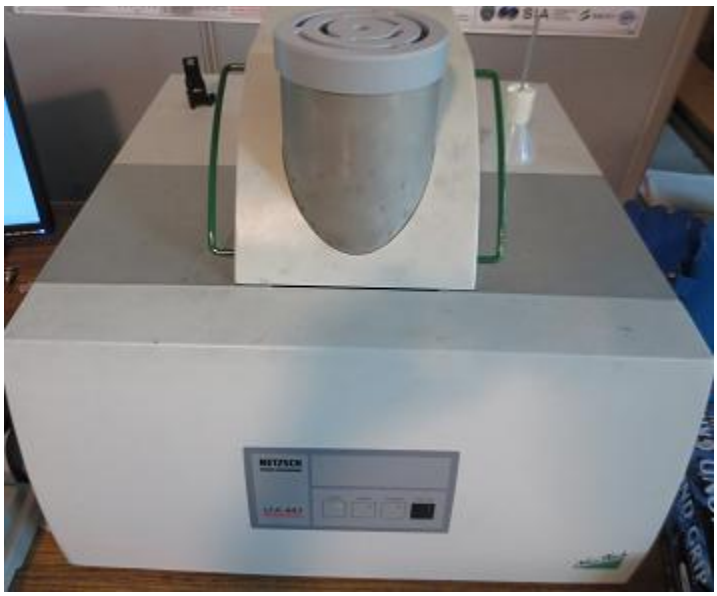

Figure 2-1 Image of LFA 447 instrument in the POEM Center, UC Riverside.

LFA 447 uses a Xenon flash lamp as a heat source. The sample is heated on one side and an InSb IR detector is used to measure the temperature the rise on the backside. This data is recorded and converted to a voltage signal which is then displayed in a plot

on-screen. Figure 2-2 [1] is an example of how this data is represented. The Nano Flash software uses one of several approximations to calculate the thermal diffusivity. The adiabatic approximation is the simplest and will be used to explain how the thermal diffusivity is calculated. For adiabatic conditions, thermal diffusivity is calculated using the formula

$$a = 0.1388 * l^2/t_{50}, \quad (1)$$

where a is the thermal diffusivity (in mm^2/s), l is the sample thickness (in cm), and t_{50} is the time (in seconds) it took the sample to reach half the max temperature measured from the back [1]. This instrument also allows for temperature control, allowing thermal diffusivity at varying temperature to be recorded.

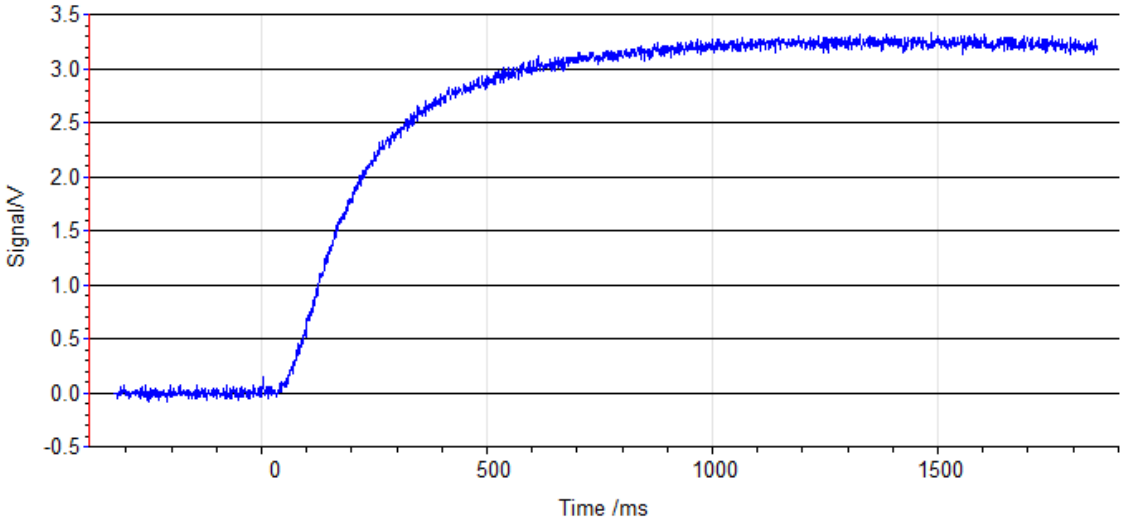

Figure 2-2 Backside sample temperature is converted to an electrical signal and is displayed as shown. Using this signal, the half rise time (t_{50}) and sample geometry, thermal diffusivity is obtained.

Thermal conductivity (out-of-plane) can be calculated using the sample's measured thermal diffusivity, bulk density, and specific heat (using either the literature or measured values).

Specific heat can also be measured with the help of a reference sample of comparable thermal diffusivity. Nano Flash software uses the general formula for specific heat, $Q = mC\Delta T$, where Q is energy, m is the sample mass, C is the specific heat of the sample, and ΔT is change in sample temperature. Q is the same for both the reference (Q_R) and sample (Q_S); therefore, specific heat of the sample (C_S) is calculated as follows:

$$Q_R = Q_S \tag{2}$$

$$(mC\Delta T)_R = (mC\Delta T)_S \tag{3}$$

$$C_S = (mC\Delta T)_R \,/\, (m\Delta T)_S. \tag{4}$$

The working principle behind the LFA 447 instrument used in this dissertation research is depicted in Figure 2-3below.

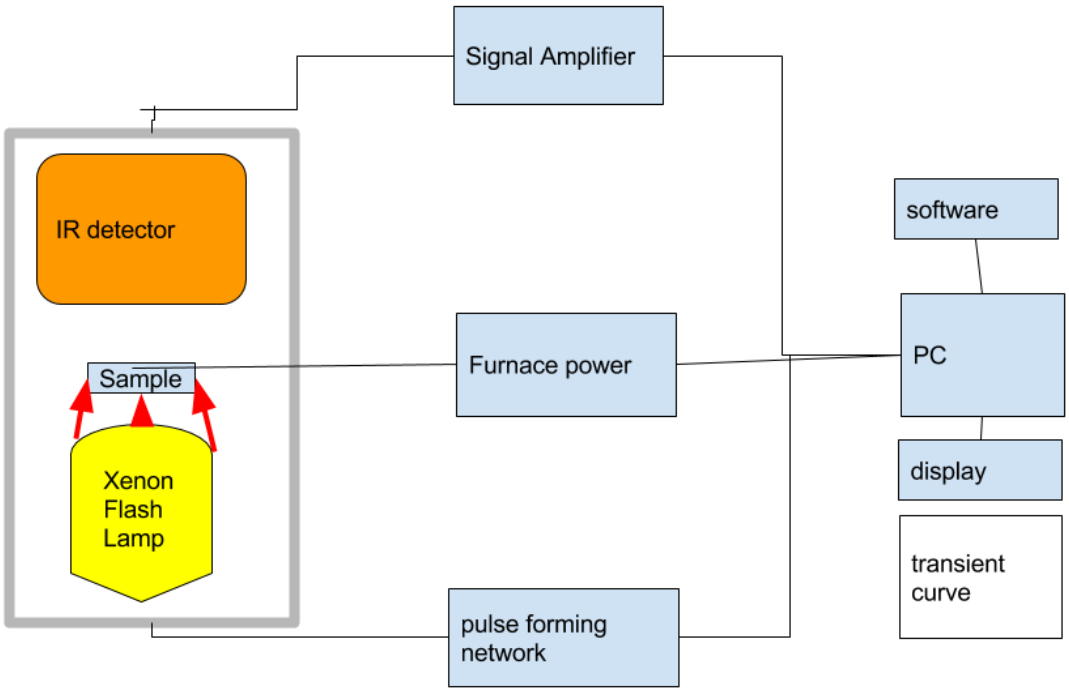

Figure 2-3 Working principle of LFA 447 instrument. A Xenon flash lamp heats up a sample from the bottom side. IR detector measures temperature rise on the opposite side of the sample. Data is converted to the voltage signal and displayed on-screen.

2.2 Hot Disk Method

The Hot Disk method is based on a transiently heated in-plane sensor [2]. The sensor consists of two double spiral thin Nickel films, see Figure 2-4 [2]. A large current passes through the sensor section heating up the sample. A sense current passes through the other spiral and acts as a temperature monitor. The sensor acts as both the heat source

and thermocouple during measurements [2]. This instrument measures the thermal conductivity, thermal diffusivity and specific heat.

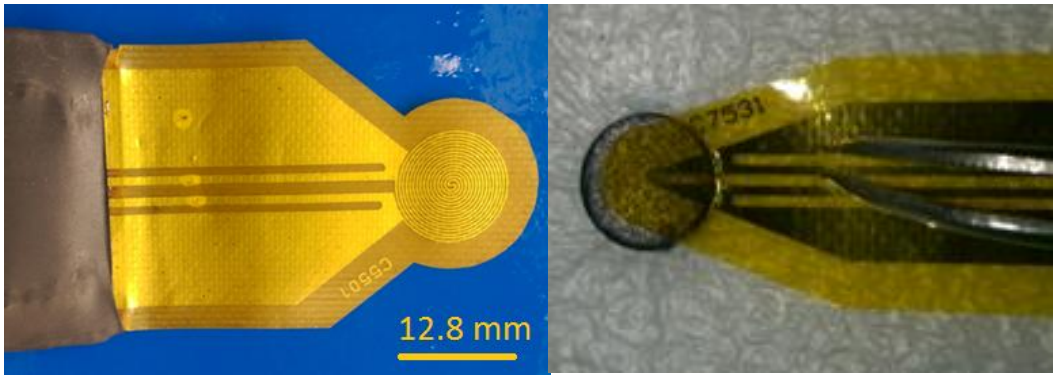

Figure 2-4 Sensor is shown on the left. The right panel demonstrates how the sensor (1 mm radius) is to be used in an experiment.

The experimental setup requires the sensor to be placed between two pieces of the material to be measured, see Figure 2-4 [2]. This is because the principle behind the Hot Disk is the assumption that the sensor in placed inside a material of infinite size to make external influences negligible [2]. In order to ensure this assumption is met, the two sample sizes must be large for this assumption to hold true. Sufficient pressure must be applied to these surfaces in order to minimize the influence of air gaps that might get trapped between the sensor and sample surfaces. To ensure greater accuracy, the surface roughness of the sample should be an order of magnitude smaller than the sensor radius.

This instrument relies on the thermal coefficient of resistivity (TCR) of the Nickel sensor for accurate measurements. The change in resistance is modeled by the function

$$\mathrm{R(t)} = R_0\{1 + \alpha * [\Delta T_i + \ \Delta T_{avg}(\tau)]\} \quad (5),$$

where R_0 is the nominal sensor resistance, α is the TCR, ΔT_i is the measure of "thermal contact" between sensor and sample surfaces, and ΔT_{avg} is the temperature rise of the sample surface [2].

$$\Delta T_{avg}(\tau) = P_0 \pi^{-3/2} (r\Lambda)^{-1} D(\tau) \quad (6),$$

where P_0 is the total power output from the sensor, r is the radius of the disk, Λ is the thermal conductivity of the sample and $D(\tau)$ is a dimensionless time dependent function with $\tau = \sqrt{(t/\Theta)}$ (7),

t is the time from the start of the transient recording, Θ is the characteristic time modeled as $\Theta = r^2/k$, (8),

where k is the thermal diffusivity of the sample. Finally, a plot of the recorded temperature versus $D(\tau)$ gives a straight line with intercept = ΔT_i, and slope = $P_0 \pi^{\frac{3}{2}} (r\Lambda)^{-1}$. Thermal conductivity is calculated through an iteration process [2].

Figure 2-5 Image of a Hot Disk instrument in the POEM Center, UC Riverside.

2.3 Differential Scanning Calorimetry

Although the Hot Disk and Laser Flash instruments are capable of measuring specific heat, these transient methods do not provide sufficient accuracy for a range of materials and sample sizes. The Laser Flash instrument has several sources of error: energy delivery to the sample varies between measurements, reflections from intervening media, and other sources. Hot Disk operates under the assumption of negligible heat losses during measurements [3] because it assumes to be inside an infinite medium. Because these two instruments mainly measure thermal diffusivity, a more accurate measurement

of specific heat is necessary for accurate thermal conductivity calculations. A differential scanning calorimeter (DSC) more accurately measures the specific heat of materials.

Figure 2-6 Image of Polyma DSC 214 calorimeter in the POEM Center, UC Riverside.

For this dissertation research, I was using Polyma DSC 214 by Netzsch, shown in Figure 2-6. DSC operates by placing two samples, one reference and the other to be measured, inside a chamber. The two samples are then subjected to a controlled heating program. The difference in heat flow to the reference and sample are monitored with respect to time [4]. The operating principle behind the Polyma DSC 214 is shown in Figure 2-7 [3].

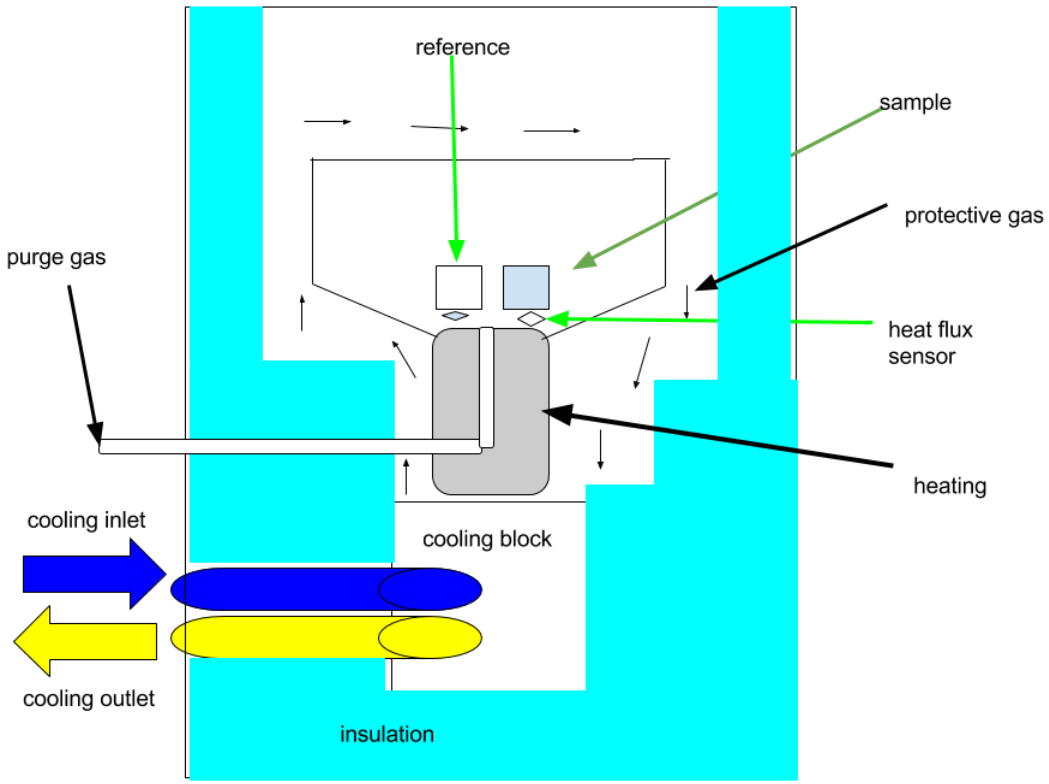

Figure 2-7. Polyma DSC 214 operates by delivering a known amount of energy to two crucibles, one empty and the other containing a material, and measuring the difference in amount of energy absorbed by each crucible. Using this difference and the specific heat of a well-known reference material, the specific heat of the sample is calculated.

In order to conduct accurate measurements, three tests must be performed: baseline, sapphire reference, and sample. Baseline measurements are performed by placing two empty crucibles into the chamber and performing a test. Afterwards, the reference materials is placed into the sample crucible (reference crucible is usually empty during tests) and another test is performed. The reference material provided is sapphire (monocrystalline alumina) [3]. This test provides the sensitivity in measuring the specific heat of desired samples. The sapphire is then removed and replaced by the desired

sample and the final test is performed. The specific heat is calculated using following equation taken from the Polyma DSC 214 manual supplement [5]:

$$c_p = \frac{\text{SD (Sample} - \text{Baseline)}}{m_s\, Q_{rate}\, s} \quad (9),$$

where SD is the signal difference, m_s is the sample mass, Q_{rate} is the heating rate, and s is the sensitivity. The sensitivity is derived from the sapphire measurement as follows [5]:

$$s = \frac{\text{SD(Sapphite} - \text{Baseline)}}{m_{sapphire}\, Q_{rate}\, C_{pt}} \quad (10),$$

where $m_{sapphire}$ is the mass of sapphire, the reference material, and C_{pt} is the theoretical specific heat of sapphire.

2.4 Current Activated Pressure Assisted Densification (CAPAD)

The samples for this section of the dissertation research were provided by Aleksey Volodchenkov, PhD student in Prof. Garay's Advanced Materials Processing and Synthesis (AMPS) Laboratory, UC Riverside. There are a number of advantages in nanostructured permanent magnets. These advantages include: improved mechanical integrity, easier material manipulation and better magnetic properties [6]. This is accomplished by introducing length scale confinement to 3D bulk magnetic materials [6] via densification of powders. To achieve this, a current activate pressure assisted densification (CAPAD) is used. CAPAD applies both a mechanical pressure, up to 500

MPa, and a current, up to 6 kA, to densify powders [7]. Figure 2-8 shows the diagram of the operating principle behind CAPAD.

CAPAD applies a mechanical pressure on the powder while the current raises the temperature quickly, to prevent grain growth. CAPAD allows precise control temperature, pressure, and time of the densification process [8]. The mechanical load helps to reduce porosity, increase density to bulk density, while maintaining the nanostructure. The current is used to increase the temperature. CAPAD is advantages because other sintering techniques requires several hours, or even days, to achieve these nanostructured bulk materials while CAPAD can achieve this in a matter of minutes. The load and current are applied within a vacuum chamber, which can also be water cooled at a rate of 500 ^{o}C/min.

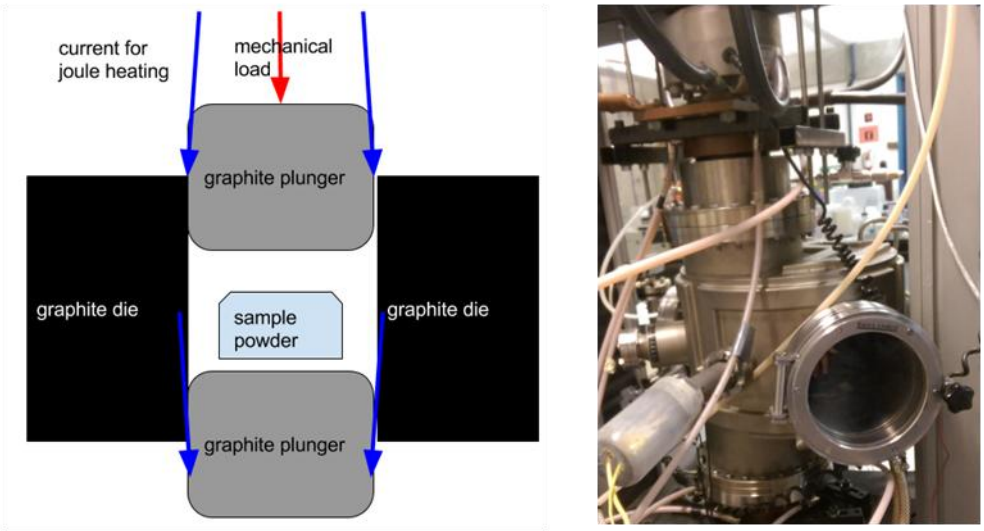

Figure 2-8 CAPAD uses a combination of Joule heating and application of mechanical load to rapidly densify powders. A photo of the CAPAD system in the AMPS Laboratory, UC Riverside is also shown.

References

[1] Netzsch LFA 447 Instruction Manual (2005)

[2] Hot Disk Thermal Constants Analyser Instruction Manual (2006)

[3] A. Berge, B. Adl-Zarrabi and C. E. Hagentroft, "*Determination of Specific Heat by Transient Plane Source*", Front. of Architec. Res. **2**, 476 (2013)

[4] Netzsch DSC 214 Polyma Manual (2013)

[5] Netzsch Specific Heat Calculation for STA: Step by Step (2013)

[6] J. R. Morales, S. Tanju, W. P. Beyermann and J.E. Garay, "*Exchange Bias in large three dimensional iron oxide nanocomposites*", Appl. Phys. Lett. **96**, 013102 (2010)

[7] J. E. Garay, "*Current Activated Pressure Assisted Densification*", Annu. Rev. Mater. Res. **40**, 445 (2010)

[8] J. R. Morales, N. Amos, S. Khizroev and J.E. Garay, "*Magneto-optical Faraday Effect in Nanocrystalline Oxides*", Jour. of Appl. Phys. **109**, 093110 (2011)

Chapter 3

Thermal Transport in $SrFe_{12}O_{19}$ [1]

Ferrites are attractive materials due to their low cost, higher operating temperatures, and abundant availability. However, magnetic and thermal properties of ferrites are not as good as those of REM. SmCo and NdFeB magnets have thermal conductivities of 12 W/mK and 9 W/mK [1-2], respectively. The ferrites' thermal conductivity are around 3 - 12 W/mK [3-5]. Thus, the strategies for replacement of REMs should include consideration of thermal properties as well. There is no reliable thermal data for $SrFe_{12}O_{19}$, which explains the selection of this material for dissertation research.

The results described in this Chapter include material characterization and measurements of thermal conductivity and thermal diffusivity of $SrFe_{12}O_{19}$ followed by relating these data to the samples' grain sizes and densities (or porosities). The axial and radial thermal conductivities are plotted against the axial and radial average grain sizes because of the anisotropic nature of the grain growth during synthesis. The thermal conductivity dependence on the mass density is also analyzed. The latter helped me to understand the effect of the grain size and density on the thermal conductivity in the material synthesized by CAPAD.

[1] Parts of this section are extracted from S. Ramirez, A. Volodchenkov, D.L. Nika, R. Samnakay, E. Uy, J.E. Garay and A.A. Balandin, *Thermal Transport in Nanostructured $SrFe_{12}O_{19}$* (in preparation, 2015)

3.1 Statistical Analysis of $SrFe_{12}O_{19}$ Grain Sizes

A set of samples was synthesized via CAPAD under different lengths of time to promote, or hinder, grain growth. The SEM study was performed to obtain the images and perform analysis of the statistical grain size distribution, see Figure 3-1. To ensure the accuracy of the statistical analysis, 100 grains were measured and taken into account for the analysis of each sample. As observed in Figure 3-1, this material exhibits highly anisotropic grain growth with a radial grain size much larger than the axial grain size. The anisotropy is observed in the distribution of grain sizes, found in table 3T-1.

Table 3T-1 Density and average grain sizes for axial and radial directions for $SrFe_{12}O_{19}$ samples

Sample ID #	radial avg. grain size (μm)	axial grain size (μm)	Density (g/cm^3)
177	0.789	0.360	4.92
178	0.733	0.202	4.41
175	1.839	0.677	4.83
179	0.698	0.224	4.68
176	1.795	0.771	4.84
174	1.028	0.609	4.91
173	0.628	0.316	4.89

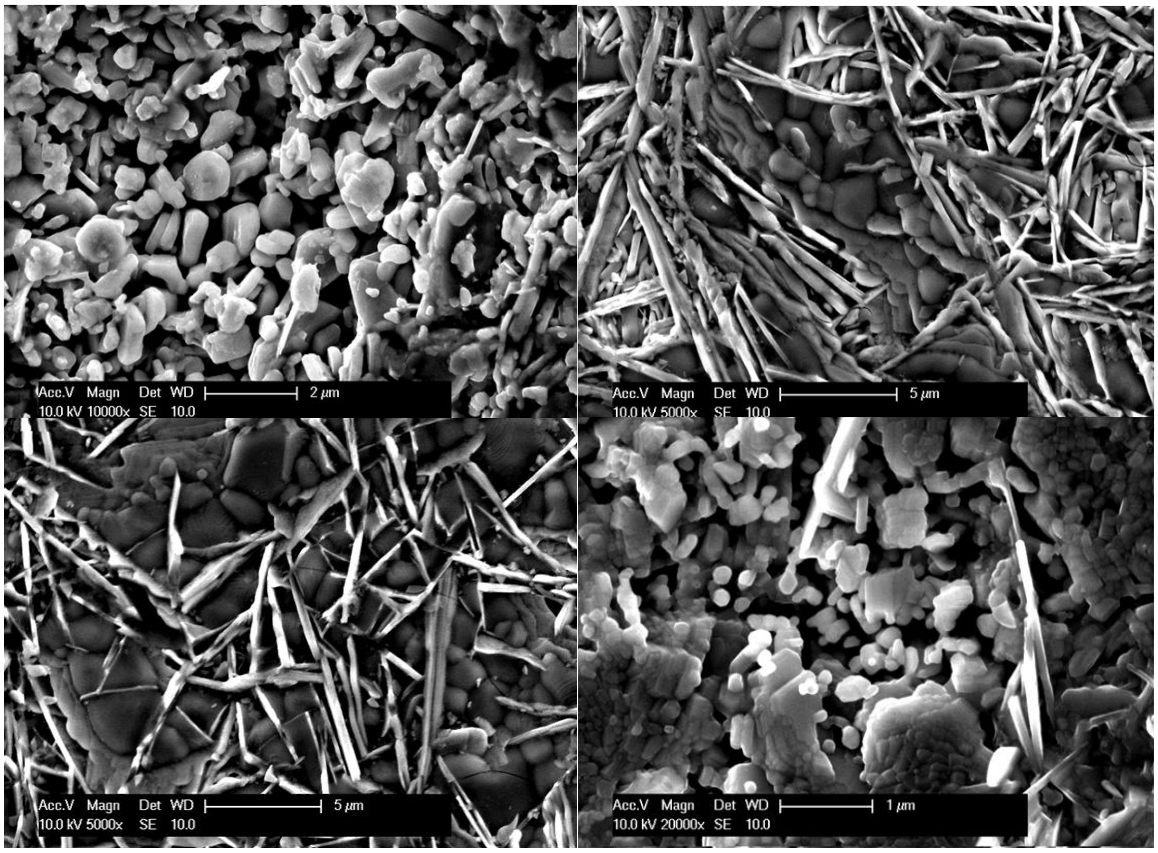

Figure 3-1 SEM micrographs of SrFe12O19 samples. a) Sample 173, b) sample 174, c) sample 177, d) sample 178. One can see that samples undergo anisotropic grain growth in varying degrees. The data is after S. Ramirez, A. Volodchenkov, D.L. Nika, R. Samnakay, E. Uy, J.E. Garay and A.A. Balandin, Thermal Transport in Nanostructured $SrFe_{12}O_{19}$ (in preparation, 2015).

3.2 Electrical Resistivity of $SrFe_{12}O_{19}$

There is a lack of data for thermal transport in permanent magnets. In many cases it is not known the relative contribution of electrons and phonons. For this reason, I studied the role of electrons in thermal transport in $SrFe_{12}O_{19}$. According to literature, $SrFe_{12}O_{19}$ is a semiconductor [8-9]. For this reason, the electron contribution to thermal transport is

expected to be lower than that of phonons but cannot be neglected for many materials. I measured the electrical resistivity for two different samples. The first sample had a density of 4.87 g/cm^3 and an average grain size of 1.46 μm. The second sample had a density of 3.99 g/cm^3 and an average grain size of 1.17 μm. Electrical resistivity measurements were performed using the van der Pauw four probe measurement method [6]. For this measurement, four probes are placed on a sample and current is passed through probes while a differential voltage is measured across the other two probes [6]. From multiple measurements like this, the sheet resistance can be calculated by dividing the measured differential voltage by the measured source current. The results obtained from performing this measurement on these samples yielded a sheet resistance ranging from 2.26 MΩ/□ to 2.43 MΩ/□, which is two orders of magnitude lower than previously reported [7], however, the resistivity is still high.

Using the sheet resistance measurements, the electron contribution to thermal transport can be determined via the Wiedemann-Franz law. This law relates the material's electrical conductivity to its electron contribution to thermal conductivity using the following relation:

$$\frac{k}{\sigma} = \frac{T}{3} * \left(\frac{\pi k_B}{e}\right)^2 \quad (11),$$

where k is the electron contribution to thermal conductivity, T is temperature, k_B is the Boltzmann constant, e is electron charge, and σ is the electrical conductivity. Using this relation, the electron contribution to thermal transport was calculated to be in the range

from 2.28 x 10^{-9} to 1.45 x 10^{-10} W/mK. This low contribution indicates that thermal transport in $SrFe_{12}O_{19}$ at room temperature is not electron dominated. The phonons are the main heat carries in this materials at room temperature.

3.3 Thermal Diffusivity and Thermal Conductivity of $SrFe_{12}O_{19}$

Thermal transport in permanent magnets has not been studied sufficiently well. Therefore, thermal transport measurements were performed on $SrFe_{12}O_{19}$ for transport in both the axial and radial directions. Axial thermal transport measurements were performed using the Laser Flash technique (LFT). With the LFT, the thermal diffusivity measurement is absolute. Thermal conductivity can then be calculated using the formula:

$$k = C_p \, \rho \, \alpha \qquad (12),$$

where C_p is the specific heat, ρ is the bulk density, α is the thermal diffusivity, and k is the thermal conductivity. The densities of these samples were calculated simply by measuring its mass and then dividing it by its calculated volume. The literature values for specific heat were used for these calculations. The results for the axial thermal conductivity and axial thermal diffusivity are shown in Figure 3-2. The results for the axial thermal conductivity versus grain size and the axial thermal diffusivity versus the grain size are presented in Figure 3-3. The obtained results are consistent with the data reported in Ref. [11].

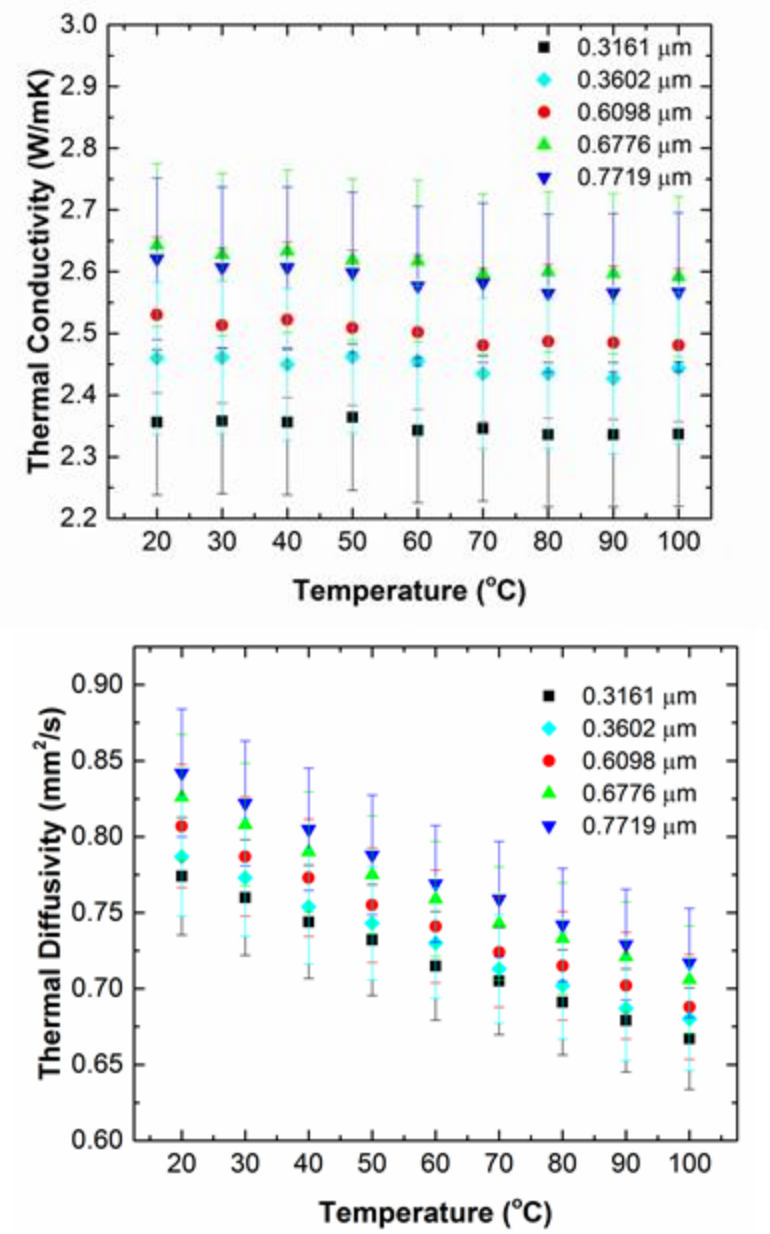

Figure 3-2 (top) Axial thermal conductivity versus temperature for all samples. Note a weak dependence on temperature in all cases. (bottom) Axial thermal diffusivity versus temperature for all samples.

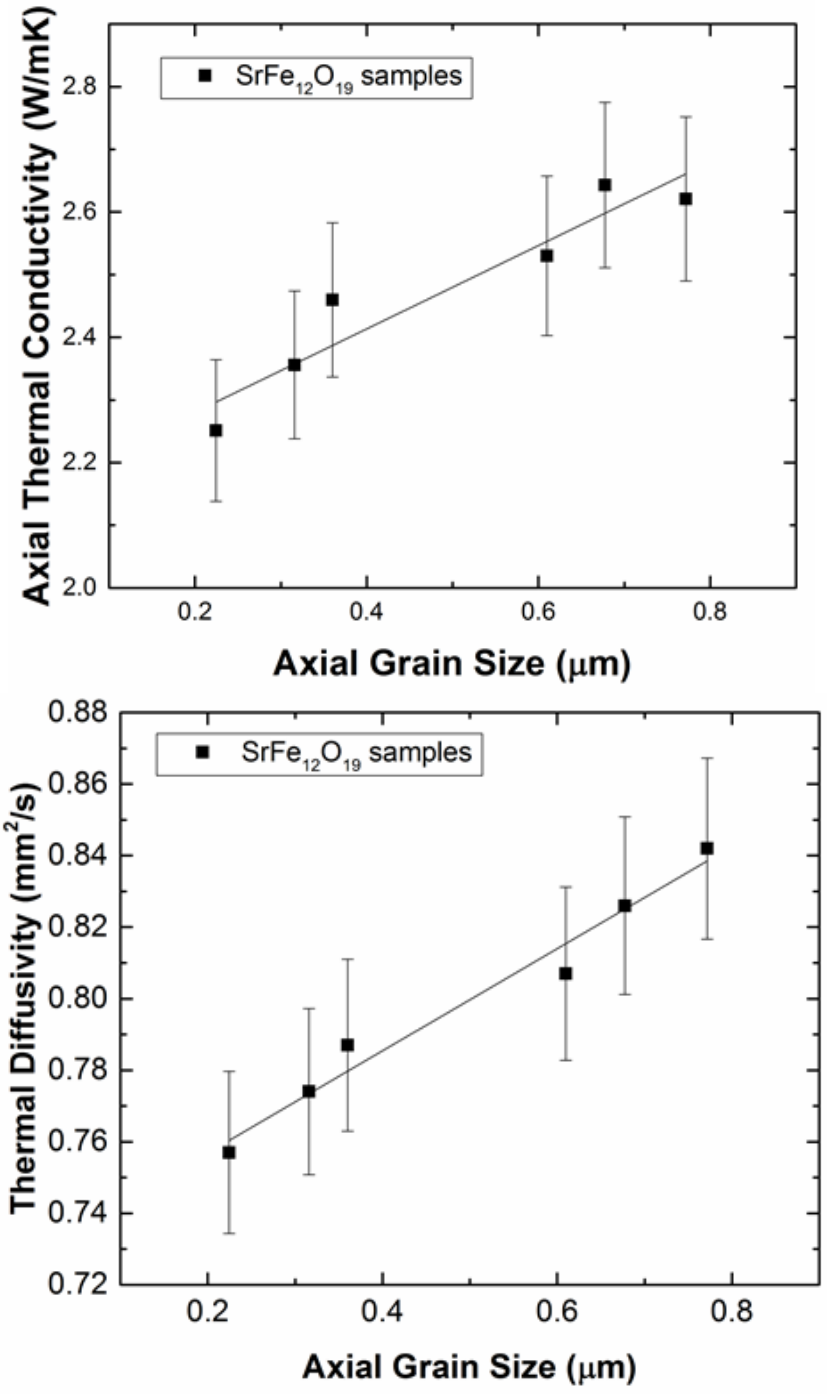

Figure 3-3 (top) Axial thermal conductivity versus the axial grain size for the samples of similar mass densities (>4.85 g/cm3). (bottom) Axial thermal diffusivity versus the axial grain size for the samples of similar mass densities (>4.85 g/cm3).

The radial thermal transport measurements were performed using the Hot Disk transient plane source method. The Hot Disk method calculates radial thermal conductivity and thermal diffusivity using only one measurement. Since this experimental setup required the use of the single sided experiment, the specific heat was needed in order to perform the calculations. The literature values for specific heat were used for these measurements. The radial thermal conductivity versus temperature and the radial grain size are shown in Figures 3-4 and 3-5, respectively.

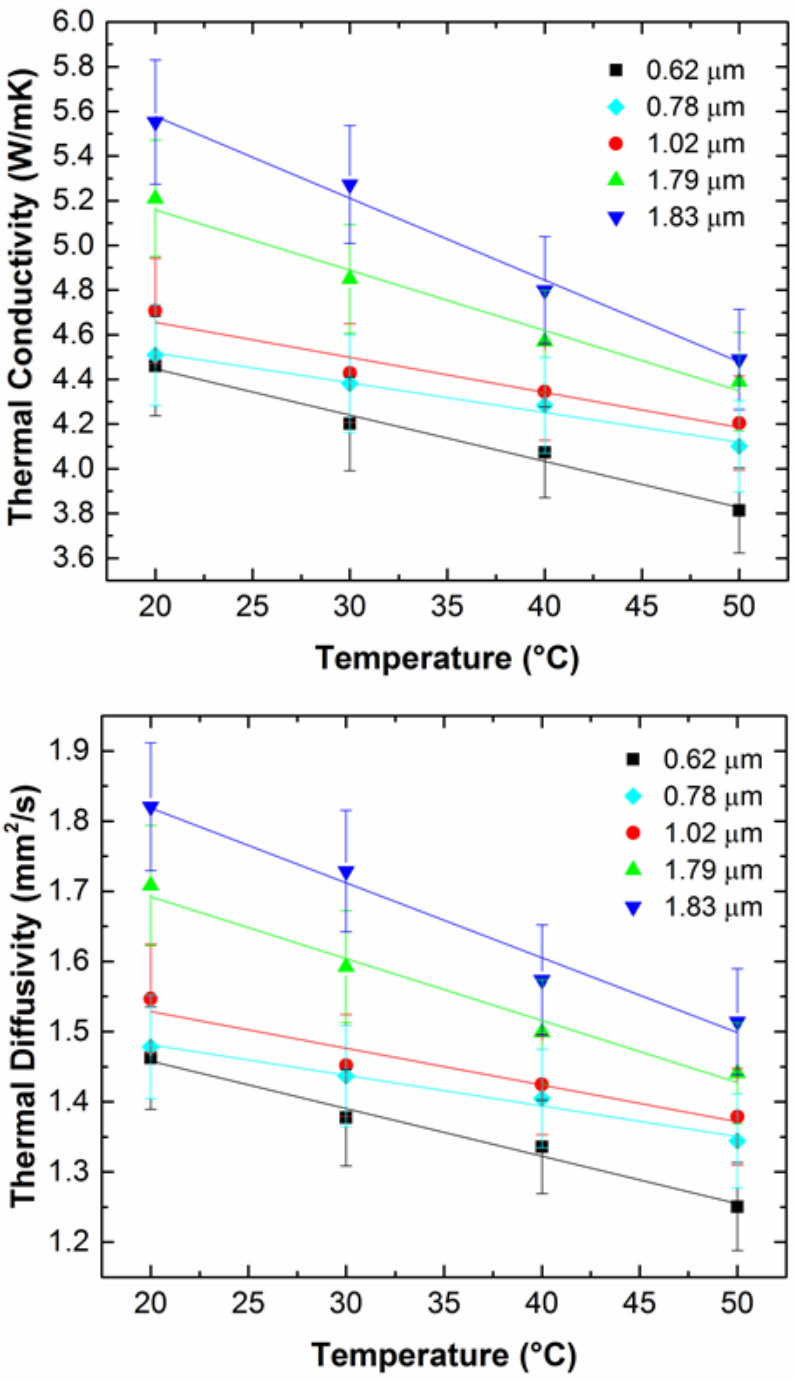

Figure 3-4 (top) Radial thermal conductivity versus temperature for the samples of similar mass density (4.85 g/cm3). (bottom) Radial thermal diffusivity versus temperature for the samples of similar mass density (4.85 g/cm3).

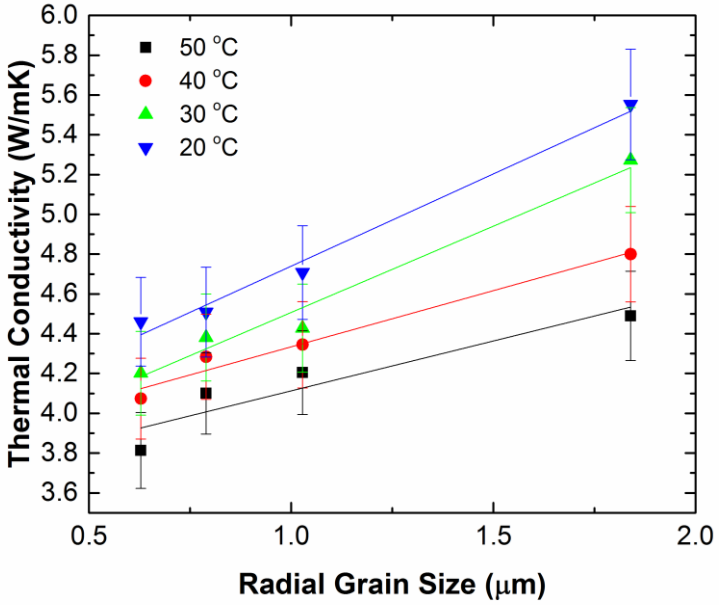

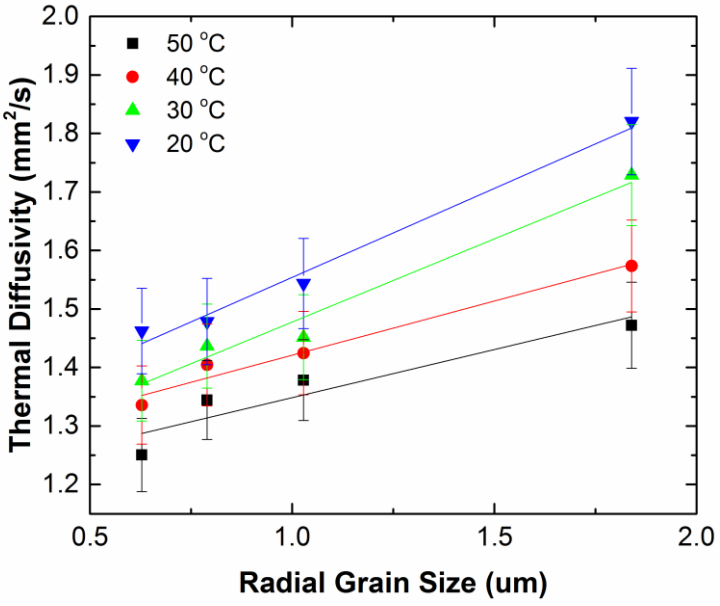

Figure 3-5 (top) Radial thermal conductivity versus the radial grain size for samples of similar mass density (4.85 g/cm3). (bottom) Radial thermal diffusivity versus the radial grain size for the samples of mass similar density (4.85 g/cm3).

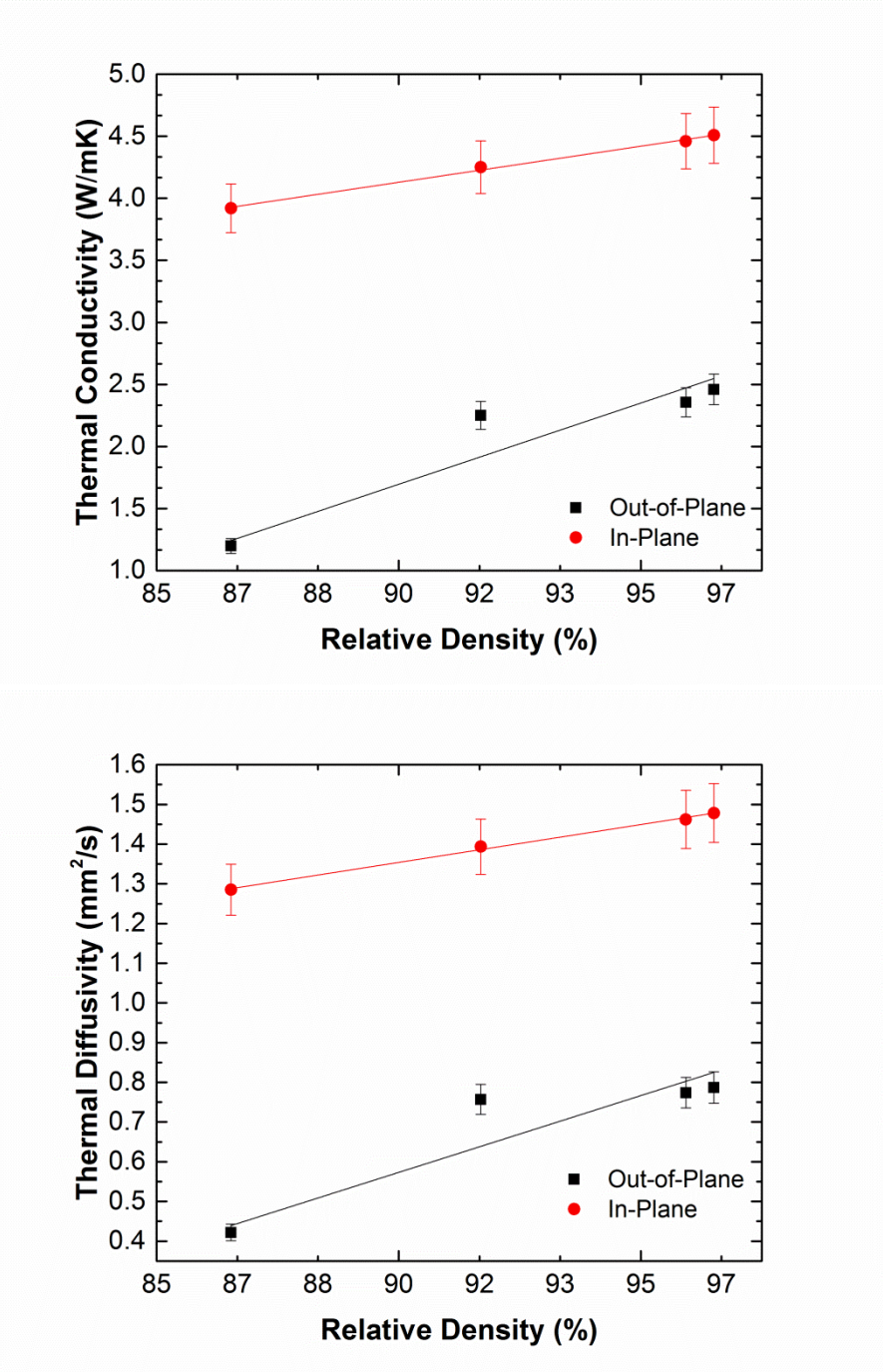

Figure 3-6 (top) Thermal conductivity versus the relative density for the samples with similar grain sizes. (bottom) Thermal diffusivity versus the relative density for the samples with similar grain sizes. The axial and radial grain sizes range from 0.2 μm – 0.36 μm and 0.62 μm – 0.78 μm, respectively.

3.4 Raman Spectroscopy of $SrFe_{12}O_{19}$

Raman spectroscopy was used as a metrology tool to verify the quality of these samples. It was performed on the samples prepared at different temperatures, 800 ^{o}C, 900 ^{o}C, and 1000 ^{o}C. Measurements results are shown in Figure 3-7. The characteristic peaks reported in literature [7], 325 cm^{-1}, 410 cm^{-1}, 519 cm^{-1}, 609 cm^{-1}, and 680 cm^{-1}, appear in our spectra, however, there are also a few extra peaks at 285 cm^{-1} and 470 cm^{-1}. Raman data for this material is scarce and I must rely on Raman studies performed on $LaFe_{12}O_{19}$ [10] because it is identical in crystal structure. The peak at 285 cm^{-1} is attributed to the E_{1g} optical phonon mode, also present in $LaFe_{12}O_{19}$ [10], and the peak at 470 cm^{-1} is attributed to the stretching modes of the FeO_6 octahedra, also present in $LaFe_{12}O_{19}$ [10].

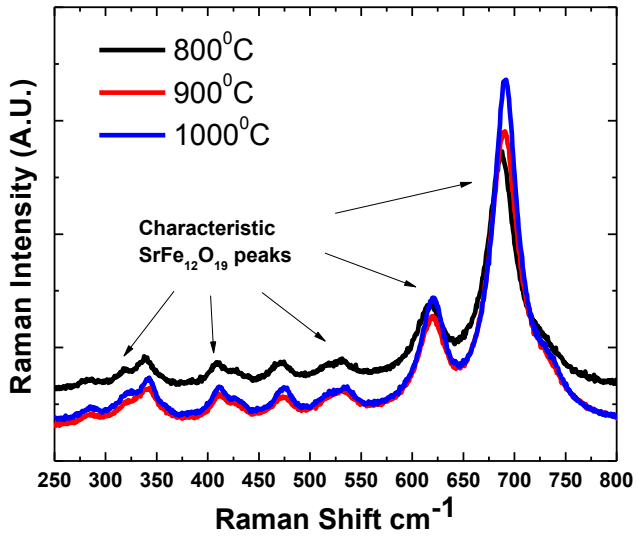

Figure 3-7 Raman spectra of SrFe12O19. The characteristic peaks are found at 285 cm^{-1}, 335 cm^{-1}, 410 cm^{-1}, 470 cm^{-1}, 519 cm^{-1}, 609 cm^{-1}, and 680 cm^{-1}.

3.5 Discussion

It is observed from Figures 3-2 and 3-4 that thermal diffusivity and thermal conductivity monotonically decrease with increasing temperature. The sample with the lowest axial thermal conductivity is the one that has the lowest mass density (4.68 g/cm^3) and smallest axial grain size (axial 224 nm). All other samples exhibit similar trends of decreasing thermal conductivity and thermal diffusivity with decreasing mass density and axial grain sizes (see Figures 3-3 and 3-5). In Figures 3-3 and 3-5, one can see that the thermal conductivity and thermal diffusivity increase monotonically with the increasing grain size. This is in line with the general trends characteristic for the boundary scattering limited thermal transport. In these samples the grain boundary scattering is clearly the dominant scattering mechanism. The anisotropic nature of heat transport is also observed with the substantially larger radial (in-plane) thermal conductivity than the axial (out-of-plane) thermal conductivity. The anisotropy in heat conduction is correlated with the anisotropic shape of the grains. Figure 3-1 reveals the anisotropic grain growth. The data is summarized in table 3T-2. In Figure 3-6, it is also observed that thermal conductivity is highly dependent on the mass density. The thermal conductivity increases monotonically with the increasing density. This is because the samples with larger mass density (lower porosity) have fewer pores that act as scattering sites for phonon transport. From the other side, the pores by themselves are low-thermally conductive voids that reduce the overall thermal conductivity of the composites.

Table 3T-2 Radial and axial thermal conductivity data for $SrFe_{12}O_{19}$ samples prepared via CAPAD

Sample ID	Radial Thermal Conductivity (W/mK) @ 20 °C	Axial Thermal Conductivity (W/mK) @ 20 °C
177	4.51	2.46
178	1.23	1.198
175	5.55	2.643
179	2.25	2.251
176	5.21	2.621
174	4.71	2.53
173	4.46	2.356

Figures 3-1 and 3-7 confirm that these samples have not undergone any type of reduction, oxidation, or reaction during or after CAPAD synthesis. For this reason, the obtained results reflect a purely $SrFe_{12}O_{19}$ nanostructured bulk sample with little to no impurities, pores excepting. It appears that thermal transport in $SrFe_{12}O_{19}$ is lower than other REMs, such NdFeB or SmCo.

3.6 Summary

In conclusion, the thermal conductivity and thermal diffusivity measurements were performed on $SrFe_{12}O_{19}$ nanostructured bulk samples. A study of the effect of the grain size, density (porosity), and temperature on thermal conductivity and thermal diffusivity

was carried out. It is observed that thermal transport (axial and radial) scales monotonically with the grain size (axial and radial) and density, and decreases with the increasing temperature. These results are important for thermal management of PMs, specifically in applications where $SrFe_{12}O_{19}$ will be used as replacement for REMs.

References

[1] S. K. Pal, "Design *Criteria for Brushless DC Motors with Hollow Rotor Of Samarium Cobalt For Applications Above 25000 RPM In Vacuum*," *Fifth International Conference on Electrical Machines and Drives,* Conf. Pub. No **341** (1991)

[2] H. Jussila, P. Salminen, A. Parviainene, J. Nerg and J. Pyrhonen, " *Concentrated winding axial flux permanent magnet motor with plastic bonded magnets and sintered segmented magnets*," *Proceedings of the 2008 International Conference on Electrical Machines*, 1(2008)

[3] H. Shen, J. Xu, A.Wu, J. Zhao and M. Shi, "*Magnetic and Thermal Properties of Perovskite $YFeO_3$ Single Crystals*," Mater. Sci, and Eng. B **157**, 1 (2009)

[4] J. Lis and P. 0. Kellard, "*Measurements of the thermal conductivity of thin films of magnetite*," Brit. J. Phys. D **2**, 1117 (1968)

[5] G. A. Slack, "*Thermal Conductivity of MgO, AlO_s, $MgA10_4$, and $Fe0_4$ Crystals from 3 to 300 K*," Phys. Rev. **126**, 427 (1962)

[6] L. J. van der Pauw, "*A Method of Measuring Specific Resistivity and Hall Effect of Discs of Arbitrary Shape*," Philips Res. Rep. **13**, 1 (1958)

[7] L. Zhang and Z. Li, "Synthesis *and characterization of $SrFe_{12}O_{19}/CoFe_2O_4$ Nanocomposites with core-shell structure*," Jour. of Alloys and Comp. **469**, 422 (2009)

[8] C. M. Fang, F. Kools, R. Metselaar, G. de With and R. A. de Groot, "*Magnetic and electronic properties of strontium hexaferrite $SrFe_{12}O_{19}$ from first-principles calculations*," J. Phys.: Condens. Matter **15**, 6229 (2003)

[9] M. J. Iqbal and M. N. Ashiq, "*Physical and electrical properties of Zr–Cu substituted strontium hexaferrite nanoparticles synthesized by co-precipitation method*," Chem. Eng. Jour. **136**, 383 (2008)

[10] J. Kreisel, G. Lucazeau and H. Vincent, "*Raman Spectra and Vibrational Analysis of $BaFe_{12}O_{19}$ Hexagonal Ferrite*," Jour. of Sol. State Chem. **137**, 127 (1998)

[11] B. Weidenfeller, M. Hofer and F. R. Schilling, "*Thermal conductivity, thermal diffusivity, and specific heat capacity of particle filled polypropylene*," Composites: Part A **35**, 423 (2004)

Chapter 4

Phonon Engineering of Fe_3O_4 using Carbon Fillers[2]

Attractive features of ferrites have already been discussed in this work, and the most well-known and widely studied of the ferrites [1] is Fe_3O_4, or magnetite (iron oxide). Magnetite is a soft ferrimagnetic material (60 - 80 emu/g) with a low coercivity [2]. One common observation with magnetic systems is the high temperatures that many PM must operate in. In addition to operation to elevated temperatures, PMs will also heat up as a result of regular use. The magnetization will degrade at higher temperatures until it reaches its Curie point, at which the magnetic materials demagnetize. Due to their low thermal conductivity special care have to be taken to prevent temperature rise in PMs to avoid demagnetization due to self-heating. One solution for this problem is raise the Curie point [3-4]. In this dissertation research I attempted an alternative approach of increasing the thermal conductivity for preventing the temperature rise.

The results described in this Chapter include a proposal of a model system in which carbon fillers are added to magnetite composite in order to achieve an increase in the thermal conductivity without a significant degradation of the magnetic properties. To verify the validity of this approach, the measurements relating to the magnetic, electric

[2] Parts of this section are extracted from S. Ramirez, K. Chan, R. Hernandez, E. Recinos, E. Hernandez, J. E. Garay and A. A. Balandin, *Thermal and Magnetic Properties of Densified Ferrimagnetic Composites with Graphene – Graphite Fillers* (in preparation, 2015).

properties, thermal conductivity, and composition have been carried out. Magnetite materials was chosen because it is well studied and easy to work with. Carbon was selected as the filler material because of exceptional heat conduction properties of graphite and graphene [5].

4.1 Preparation of Fe_3O_4 Samples with Carbon Fillers

Commercially purchased 20 nm grain size γ-Fe_2O_3 from Inframat Advanced Materials was used as the starting material. Carbon flakes (1 - 150 μm flakes) were acquired from Asbury Carbons while the graphene flakes (12 nm flakes) were obtained from Graphene Supermarket. The starting powders were first dispersed in ethanol and underwent ultrasonication for one hour. The ethanol solution was then evaporated at 80 ^{o}C for 12 hours. Using CAPAD, the powder was rapidly densified at 600 ^{o}C with an applied load of 150 MPa [6]. The sample synthesis for this part of the dissertation research was performed by Kyle Chan, a PhD Candidate in Prof. Javier Garay's Advanced Materials Processing and Synthesis (AMPS) Laboratory at UC Riverside.

4.2 Material Characterization

Bulk samples were analyzed using the scanning electron microscopy (SEM) in order obtain an accurate view of the samples nanostructure and to observe if any reaction occurred during CAPAD processing. SEM micrographs are shown in Figure 4-1. A

distinction between magnetite and carbon is clearly observed in the Figures, indicating that no reaction occurred between the carbon and iron oxide phases. Figure 4-1 demonstrates the nanostructure of magnetite (approximately 50 nm grains) and also the much larger flake sizes of carbon. The visual confirmation of no reaction indicates that iron oxide's magnetic properties are expected to be preserved.

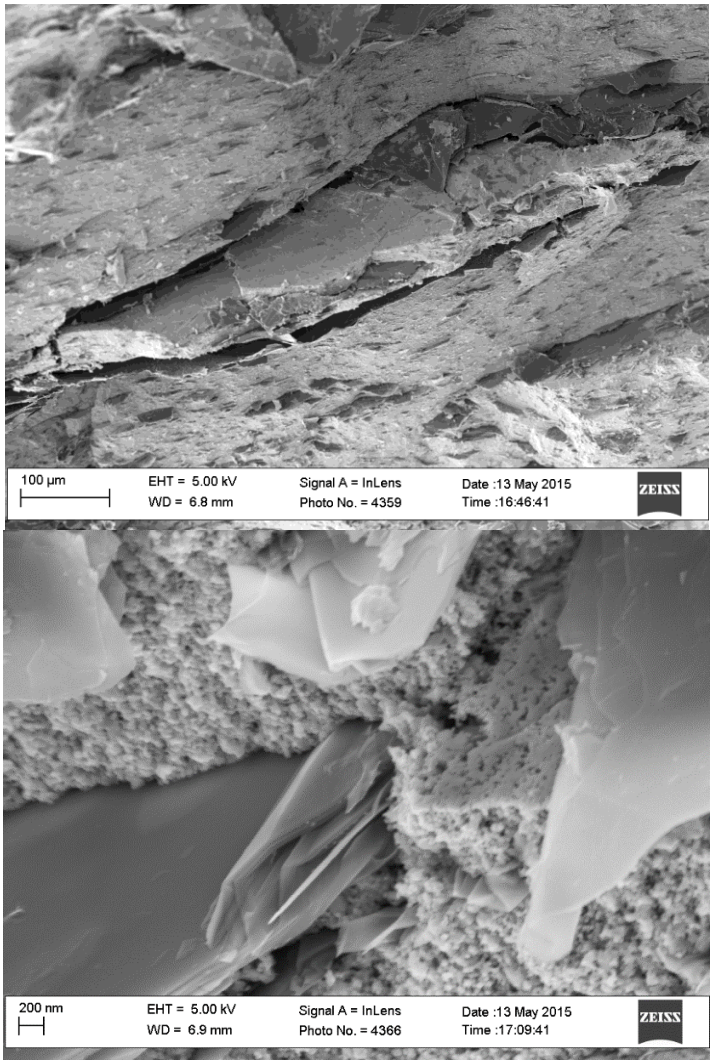

Figure 4-1 SEM micrographs of iron oxide sample with 5 wt. % graphite. (top) Graphite and iron oxide flake size differences can be easily observed. (bottom) Zoomed in image where iron oxide's nanostructured grains are easily observed. Magnetite's grains are all less than 100 nm with most grains appearing to be 50 nm in size. Note that there is clear segregation of carbon and iron oxide phases, indicating the occurrence of minimal reaction between the two phases.

To further substantiate our claim of a separation of iron oxide and carbon phases during CAPAD processing, Raman spectroscopy was performed. Raman was used as a metrology tool to verify the presence of carbon, iron oxide, and any other material that could have formed during synthesis but is not visible under SEM. Raman spectrum of magnetite with graphite fillers is seen in Figure 4-2. The peaks corresponding to magnetite and graphite are clearly observed, and in line with literature [7-8] along with a few other peaks corresponding to α-Fe_2O_3 (Hematite), which were induced by laser excitation during the measurement [9]. Again, a separation of the iron oxide and carbon phases are obvious in the data provided.

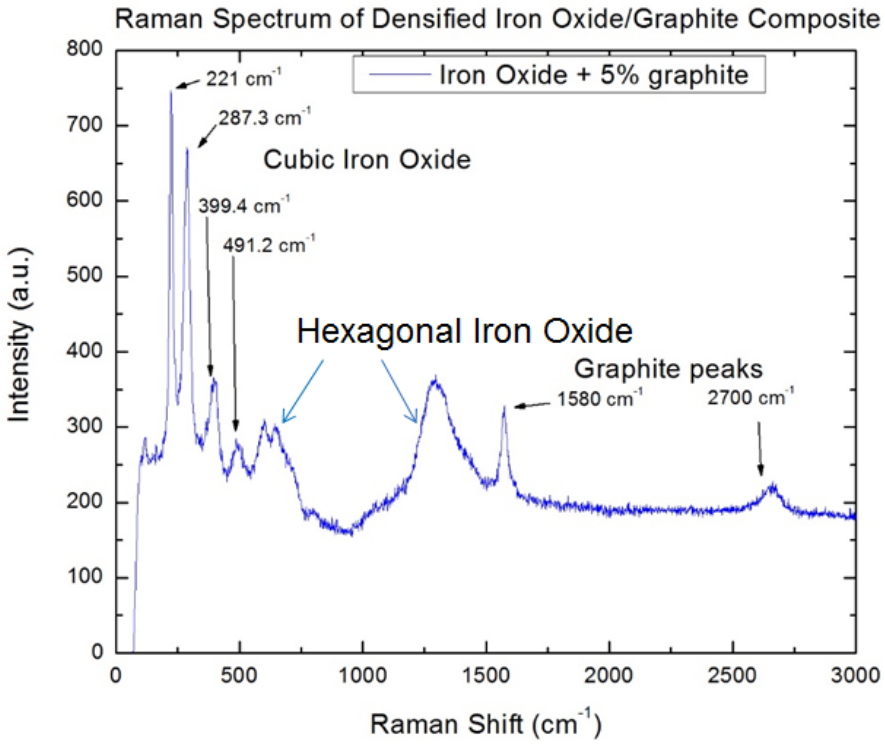

Figure 4-2 Raman spectrum of magnetite samples containing 5 wt. % graphite. The cubic iron oxide peaks are observed at 221 cm^{-1}, 287.3 cm^{-1}, 399.4 cm^{-1}, and 491.2 cm^{-1}. The graphite peaks are observed at 1580 cm^{-1} and 2700 cm^{-1}. The hexagonal iron oxide peaks are seen at 600 cm^{-1} and 690 cm^{-1}. The 1300 cm^{-1} peak is attributed to the 2nd order scattering from hexagonal iron oxide.

X-Ray Diffraction (XRD) was performed to investigate the crystallinity of the composites and further verify the segregation between carbon and magnetite. The XRD results are shown in Figure 4-3. It observed that samples containing only graphite as filler material exhibit peaks for cubic iron oxide, carbon, and a small amount of hexagonal iron oxide. Hexagonal iron oxide is present in these samples because it does not fully reduce to its cubic polymorph during CAPAD synthesis, which explains the small amount present, indicated by the small peaks in the sample containing 2 % graphite. However, for the samples containing graphene – graphite mixture fillers, the hexagonal iron oxide peaks are of similar intensity to the cubic iron oxide peaks, indicating a significant amount of hexagonal iron oxide. I believe the presence of such a large amount of hexagonal iron oxide is due to the graphene flakes acting as a barrier to reduction, thus preventing hexagonal iron oxide from fully reducing to its cubic polymorph. With such a large presence of hexagonal iron oxide, it expected that magnetic and thermal properties of this type of samples will be affected more.

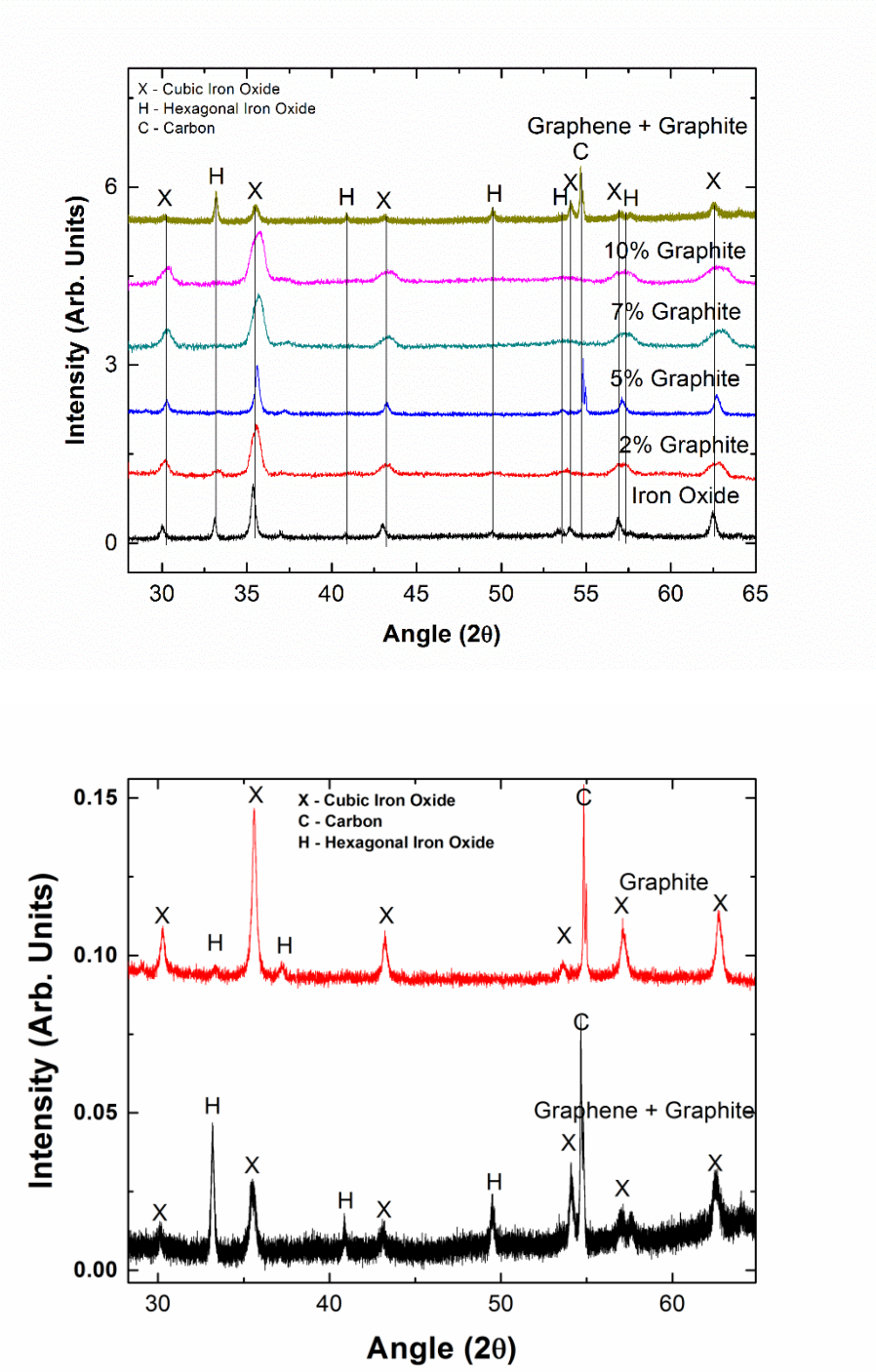

Figure 4-3 (top) XRD results for the samples showing presence of carbon, cubic and hexagonal iron oxide. Hexagonal iron oxide appears in small amounts in the sample with <5 % graphite and in the sample containing graphene-graphite mixture fillers. (bottom) Intensity of hexagonal iron oxide peak is of similar magnitude to cubic iron oxide in sample containing graphene-graphite mixture fillers. XRD validates claim that no reaction carbon and iron oxide phases occurred.

A reaction between carbon and iron oxide, thus forming an alloy, is expected from these two materials. If the reaction occurs, then we should observe a significant decline in the saturation magnetization of magnetite. In addition, the presence of hexagonal iron oxide should also affect its magnetic properties. The Vibrating Sample Magnetomoetry (VSM) was performed in order to obtain the samples' magnetic hysteresis curves to observe if such a decline occurred. Typical VSM systems rapidly vibrate a sample between two pickup coils while applying a magnetic field, creating an alternating magnetic field, thereby inducing a measureable bias. By measuring the bias, one can determine the magnetic moment of the sample at varying external magnetic fields. These samples were initially magnetized by sweeping the applied field from zero to 17kOe. The full hysteresis loop was obtained from -17kOe to 17kOe. My collaborator, Kyle Chan, performed these measurements and taught me the operating principle behind VSM along with how to use the instrument. All samples underwent this magnetizing process and we obtained their respective hysteresis curves, shown in Figure 4-4.

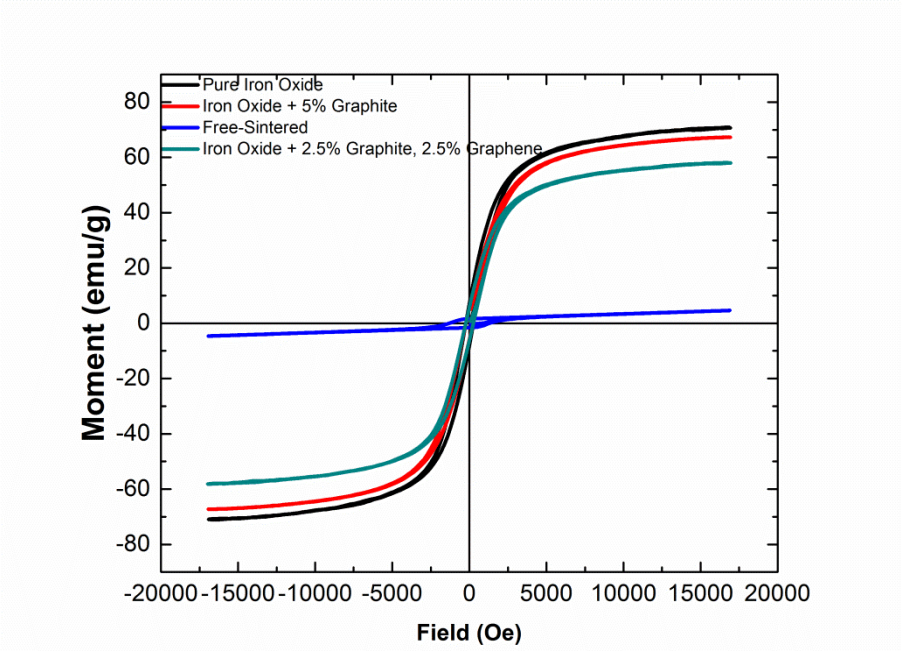

Figure 4-4 Normalized magnetic moments vs external magnetic field (magnetic hysteresis curves) obtained via VSM for pure magnetite (Iron Oxide), iron oxide + 5% graphite, iron oxide+ 2.5% graphite + 2.5% graphene, and free-sintered Iron Oxide. The saturation magnetization is within expected ranges for all samples except free-sintered Iron Oxide. The data is after S. Ramirez, K. Chan, R. Hernandez, E. Recinos, E. Hernandez, J. E. Garay and A. A. Balandin, Thermal and Magnetic Properties of Densified Ferrimagnetic Composites with Graphene – Graphite Fillers (in preparation, 2015).

In an ideal magnetic composite, the total saturation magnetization should obey a rule of mixtures by decreasing proportionally with the amount of non-magnetic material added [10-11]. It is observed that the pure iron oxide (magnetite) sample saturates around 75 emu/g and is well within the expected range for magnetite [2]. It is also observed that the iron oxide sample with graphite saturates around 70 emu/g and is also within the expected range for pure magnetite. The iron oxide sample with both graphene and graphite also appears to saturate around 60 emu/g, which is the lower range typical for pure magnetite. Therefore, the addition of small amounts of carbon fillers, even when

taking dilution effects into account, does not significantly degrade magnetite's saturation magnetization. Although, the addition of graphene-graphite mixture fillers reduces iron oxide's saturation magnetization by a large amount, the saturation magnetization is approximately on the lower range for magnetite. Therefore, it could be used in most, if not all, of its typical applications. In other words, magnetite's magnetic properties are retained. This demonstrates that the addition of carbon fillers have very little effect on magnetite's magnetic properties and can be used in their expected applications without significant penalty to its saturation magnetization. The free-sintered sample, on the other hand, demonstrates a significant reduction to magnetite's saturation magnetization indicating that some form of reaction between the carbon and iron phases occurred and, thus, losing some of its composite nature. This also demonstrates CAPAD's unique sintering ability to get around certain natural processes and create composites not possible in traditional sintering methods. These are promising results in terms of heat conduction that will be verified later in this text.

4.3 Electrical Resistivity and Electron Contribution to Thermal Conductivity

We have demonstrated that our samples retained their magnetic properties and their composite nature; therefore, we should investigate next whether the addition of carbon flakes altered our samples' electrical conductivity. Magnetite is a semiconductor, almost metallic, with sheet resistivity ranging from 1 - 1k Ω/□ [2]. It is well known that graphite is a conductor with an electrical conductivity of 200 $(\Omega\text{-cm})^{-1}$ [12] at room temperature

and it was shown graphene is a good electrical conductor, with an electrical conductivity of 10^5 $(\Omega\text{-cm})^{-1}$ [13]. Thus, the addition of carbon fillers, either graphene or graphite, could increase magnetite's electrical conductivity, which could result in a less desirable magnet.

Electrical resistivity measurements were performed using the Van der Pauw technique [14]. The Van der Pauw technique is a four probe measurement that applies a current between two probes and measures the voltage induced. From this, a material's sheet resistance is calculated. The resistivity can be calculated by multiplying the sheet resistance by the sample's thickness. This measurement was performed for pure magnetite, magnetite + 5% graphite, and magnetite + 2.5% graphite + 2.5% graphene. We measured resistivities of 3.89, 5.83, and 3.84 (Ω-m) for magnetite, magnetite + 5% graphite, and magnetite + 2.5% graphite + 2.5% graphene, respectively. The resistivity obtained for pure magnetite is consistent with literature and is expected due to its nearly metallic nature. It is observed that the electrical resistivities for the samples containing carbon are relatively unchanged in comparison to pure magnetite. As a result, the 5% of carbon by weight added does not create an interconnected network where the percolation threshold is exceeded. Therefore, not only do the samples retain their composite nature and magnetic properties, their electrical properties also remain unchanged. The addition of small amounts of carbon fillers into our composite samples did not seriously alter their magnetic and electric properties.

The electron contribution to the thermal conductivity was calculated using the Wiedemann-Franz law, previously described in Chapter 3, using the resistivity values

obtained from our measurements. The electron contribution was determined to be around 1.22 – 1.9 μW/mK which is less than 1 % of the total measured thermal conductivity. Therefore, heat transport in our samples, with or without carbon, is phonon dominated in the examined temperature range.

4.4 Thermal Conductivity Enhancement of Iron Oxide with Carbon Fillers

Having established our samples' composite nature, magnetic, and electrical properties, we present the measured thermal conductivities for both in-plane and out-of-plane of each sample. The out-of-plane thermal conductivity was measured using the Laser Flash method. The Laser Flash method works by using a flash lamp to heat up one side of the sample and measures the temperature rise on the backside of the sample using an IR detector. From the temperature rise and sample thickness, the thermal diffusivity can be obtained. Using the thermal diffusivity, the thermal conductivity can be calculated. Iron oxide samples containing 5 %, 7 %, and 10 % of carbon fillers were measured using this method. Temperature dependent results are shown in Figure 4-5.

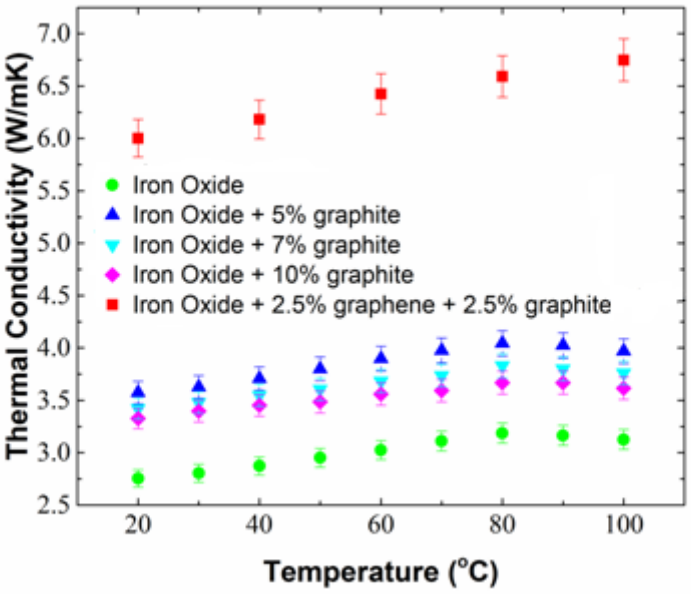

Figure 4-5 Out-of-plane thermal conductivity versus temperature for magnetite samples containing 0, 5, 7, and 10 % carbon fillers. The largest enhancement of the thermal conductivity occurs in the sample that contains graphene-graphite mixture fillers. The data is after S. Ramirez, K. Chan, R. Hernandez, E. Recinos, E. Hernandez, J. E. Garay and A. A. Balandin, Thermal and Magnetic Properties of Densified Ferrimagnetic Composites with Graphene – Graphite Fillers (in preparation, 2015).

It is observed that out-of-plane thermal conductivity for magnetite increases with the addition of carbon fillers. The largest enhancement of the thermal conductivity achieved in the samples with graphene and graphite mixture (enhancement of 120%), followed by the sample with 5% graphite (enhancement of 29%), and lower enhancement in the samples containing 7 % and 10 % graphite. These results are promising because the examined samples have not experienced significant degradation of magnetic properties but demonstrated improvement in the out-of-plane thermal conductivity. Since the samples containing >7 % carbon demonstrated significant reduction in saturation magnetization, only the samples containing 5 % carbon were analyzed further.

Magnetite has a cubic based, inverse spinel crystal structure. This implies that heat transport is isotropic in magnetite. However, due the highly anisotropic hexagonal crystal structure of carbon, in-plane thermal conductivity was measured to verify if the thermal conductivity enhancement was also anisotropic. The in-plane thermal conductivity measurements were performed using the Transient Plane Source (TPS) technique. TPS operates by placing a two spiral sensor in between two sample pieces, applying heat through one spiral, and measuring the temperature rise of the sample through the other spiral. The sensor acts as both a heat source and thermometer. From this method, both the in-plane thermal diffusivity and thermal conductivity are obtained through a single measurement. In-plane thermal conductivity for magnetite samples at room temperature (20 ^{o}C), along with their respective thermal conductivity enhancements, are shown in table 4T-1. Anisotropic enhancement of in-plane thermal conductivity is observed with the greatest enhancement (260 %) belonging to the sample containing graphite and graphene. These results indicate that an enhancement of thermal conductivity can be achieved by the addition of carbon fillers with very little cost to other desired properties in magnetite.

Table 4T-1 Thermal conductivity and thermal conductivity enhancement with their respective carbon loading fractions for magnetite samples

Sample	Loading Fraction (%)	Thermal Conductivity (W/mK)	Thermal Conductivity Enhancement (%) [kn-ki/ki]
Fe3O4	0	2.7 (cross-plane) 2.57 (in-plane)	0
Fe3O4 + graphite	5	3.55 (cross-plane) 5.4 (in-plane)	29 (cross-plane) 110 (in-plane)
Fe3O4 + graphite + graphene	5 (2.5% graphite + 2.5% graphene)	6 (cross-plane) 9.3 (in-plane)	120 (cross-plane) 260 (in-plane)

We have demonstrated that the addition of carbon fillers results in the enhancement of thermal conductivity for iron oxide. We also observed that the greatest enhancement in thermal conductivity belong to the samples with carbon content no greater than 5 % by weight.

4.5 Discussion

We have demonstrated that the addition of small amounts of carbon fillers yield an improvement in thermal conductivity without significant degradation to PM's magnetic properties. In our pure magnetite samples, phonon transport is grain boundary limited due to the nanometer scale sized grains. This conclusion is supported by the fact the

thermal conductivity of the nanostructured samples is lower than that of bulk magnetite's 4.61 W/mK [11]. In samples with graphite – graphene fillers, the phonon transport is still predominantly grain boundary limited but it is assisted by partial heat transfer via strongly thermally conductive fillers. Thermal conductivity enhancement is attributed to the carbon fillers facilitating phonon transport around the Fe_3O_4 nanostructured grains in samples containing only graphite fillers because they provide a much easier conduction path with fewer grain boundaries and interfaces. For the sample containing graphene-graphite fillers, the presence of hexagonal iron oxide can also aid in the conduction of heat. The presence of hexagonal iron oxide can be explained by graphene acting as a barrier to reduction, preventing hexagonal iron oxide to complete reduce to its cubic polymorph. Therefore, the enhancement in thermal conductivity is attributed to graphene, graphite, and hexagonal iron oxide each contributing to phonon transport. Total thermal conductivity of the carbon containing composites exceeds even that of bulk of magnetite. These results are only possible because of the separation of phases between carbon and iron oxide. The separation of carbon and Fe_3O_4 phases is only possible due to the rapid densification process using CAPAD.

These results demonstrate, as a proof of concept, that the thermal conductivity of solid systems can be increased by the addition of thermally conductivity fillers. This concept is common for polymer composites and fluids but have not been used widely with solid composite materials. We are not aware of any reported results along this line for nanostructured magnetic materials. The obtained results are important for thermal management of magnetic systems. The magnetic materials can have improved thermal

conductivity with having to sacrifice very little in other desired properties. Furthermore, these results also imply that this concept can be applied to materials beyond those described here and that certain naturally occurring phenomena, such as reactions, can be averted.

4.6 Summary

In this Chapter, we presented a concept in which carbon fillers are added to magnetic material in an effort to increase its thermal conductivity without negatively affecting its magnetic properties. It was shown that CAPAD method of sample preparation can provide desired separation of phases between carbon and iron oxide. The separation of phases was confirmed via XRD, Raman spectroscopy, and SEM. The magnetic properties of magnetite did not suffer significantly when dilution effects were accounted for in samples with 5 % carbon content. In addition to this, magnetite's electrical properties were also unchanged. As a result, an enhancement to its thermal conductivity was observed, for both in-plane and out-of-plane, with enhancements up to 260 % and 120 %, respectively. These results are important for thermal management of magnetic systems.

References

[1] C. Clauser and E. Huenges, "*Thermal Conductivity of Rocks and Minerals*," Amer. Geophys. Union 1 (1995)

[2] R. M. Cornell and U. Schwertmann, "*The Iron Oxides*", 2nd ed. Wiley-VCH, (2003)

[3] J. Navarro, C. Frontera, Ll. Balcells, B. Martinez and J. Fontcuberta, "*Raising the Curie temperature in Sr_2FeMoO_6 double perovskites by electron doping*," Phys. Rev. B **64**, 092411 (2001)

[4] M. Sagawa, S. Fujimura, H. Yamamoto, Y. Matsuura and K. Hiraga, " *Permanent Magnet Materials Based on the Rare Earth-Iron-Boron Tetragonal Compounds*," IEEE Transact. on Magnet. **20**, 1584 (1984)

[5] A. A. Balandin, S. Ghosh, W. Bao, I. Calizo, D. Tewelderbhan, F. Miao and C. N. Lau, "*Superior Thermal Conductivity of Single-Layer Graphene*," Nano Lett. **8**, 902 (2008)

[6] J. E. Garay, "*Current-Activated Pressure Assisted Densification of Materials*", Annu. Rev. of Mater. Res. **40**, 445 (2010)

[7] O. N. Shebanova and P. Lazor, "*Raman spectroscopic study of magnetite ($FeFe_2O_4$): a new assignment for the vibrational spectrum*," Jour. of Sol. State Chem. **174**, 424 (2003)

[8] F. Tunistra and J. L. Koenig, "*Raman Spectrum of Graphite*," J. Chem. Phys. **53**, 1126 (1970)

[9] O. N. Shebanova and P. Lazor, "*Raman study of magnetite (Fe_3O_4): laser-induced thermal effects and oxidation*," J. Raman Spectrosc. **34**, 845 (2003)

[10] J. R. Morales, "*Novel Magnetic Behavior in Bulk Nanostructured Iron Oxides*," no. August (2008)

[11] C.-G. Stefanita, "*Magnetism Basics and Applications*," Springer Science & Business Media, (2012)

[12] W. Primak and L. H. Fuchs, "*Electrical Conductivities of Natural Graphite Crystals*," Phys. Rev. **95**, 541 (1954)

[13] R. L. Powell and G. E. Childs, "*American Institute of Physics Handbook*," 3rd ed. *McGraw-Hill*, New York (1972)

[14] L. J. van der Pauw, "*A Method of Measuring Specific Resistivity and Hall Effect of Discs of Arbitrary Shape*," Philips Res. Rep. **13**, 1 (1958)

Chapter 5

Strongly Anisotropic Thermal Conductivity of Reduced Graphene Oxide Films Annealed at High Temperature[3]

In this Chapter we describe thermal properties of reduced graphene oxide films, which can be used for thermal management either as separate films or as fillers. Thermal management of modern electronics requires thin films with highly anisotropic thermal conductivity, where the in-plane thermal conductivity, K, is substantially larger than the out-of-plane thermal conductivity $K_{\perp}$ [1]. The function of thermal pads or coating layers with this property is to conduct heat away from the hot spots in the in-plane direction while protecting electronic components underneath them from heating. High-quality bulk graphite is an anisotropic heat conductor with the thermal conductivity along the basal planes of $K \approx 2000$ W/mK and the cross-plane thermal conductivity $K_{\perp} \approx 20$ W/mK at room temperature (RT) [2, 3]. The commercial thermal pads based on graphite have lower K and smaller $K / K_{\perp}$ ratios. These considerations create motivations for the search of new materials with high $K / K_{\perp}$ that can be used for thermal management, including the removal of excess heat (high K) and shielding from excess heat (lower $K_{\perp}$).

[3] Part of the material in this section is reproduced with permission from John Wiley and Sons publisher from the paper by J.D. Renteria, S. Ramirez, B. Alonso, A. Zurutuza, H. Malekpour, A.I. Cocemasov, D.L. Nika and A.A. Balandin, *Strongly Anisotropic Thermal Conductivity of Free-Standing Reduced Graphene Oxide Films Annealed at High Temperature, Advanced Functional Materials* 25, 4664 (2015) under license number 3742090788433 for the use in this dissertation.

The discovery that graphene has extremely high in-plane thermal conductivity, which can exceed that of the basal planes of graphite [4-8], stimulated a surge in experimental and theoretical studies of heat conduction in graphene and other two-dimensional (2-D) materials [9-14]. Graphene and few-layer graphene (FLG) layers were proposed for thermal management applications as fillers in the thermal interface materials [15-17] or flexible heat spreaders for local hot-spot cooling in electronics and optoelectronics [18-21]. One of the practically feasible ways to industry-scale applications of graphene-based materials for thermal management lies in the reduction of graphene oxide (GO). A well-established Hummers method or its modifications [22-23] allows one to mass produce GO from natural graphite. Thin films on the basis of GO have been shown to have excellent mechanical properties [24-25]. However, GO reveals very low thermal conductivity K=0.5 W/mK – 1 W/mK [26-28] at RT. The reduction of GO films to obtain the reduced graphene oxide (rGO) films via conventional chemical or thermal techniques does not necessarily results in increased K or $K/K_{\perp}$ ratio owing to residue impurities, defects and disorder [8].

Having demonstrated that graphite and graphene could both be used to improve thermal conductivity of magnetic composites, this Chapter will report our finding that annealing of the free-standing GO films at temperature, T ≈ 1000 ^{o}C, results in substantially increased in-plane thermal conductivity and, simultaneously, reduced cross-plane thermal conductivity. Anisotropy of the thermal conductivity attains a record-high value of $K / K_{\perp}$ = 675 making the flexible rGO films attractive for thermal management applications. Moreover, the exposure of rGO films to 1000 °C temperature treatment

reduces their electrical resistivity to 1–19 Ω/□, which is the smallest reported to date for such materials. The theoretical considerations suggest that the in-plane thermal conductivity and $K / K_{\perp}$ can be increased further via the control of the sp^2 grain size and oxygen residue. This makes rGO an attractive alternative for improving thermal conductivity of nanostructured bulk permanent magnets.

5.1 Analysis of Microscopy Data

The samples investigated in this study included the reference free-standing GO films and the films annealed at different temperatures: 300, 600, and 1000 °C. The temperature treatment results in reduction of GO films to obtain the free-standing rGO films. The samples were prepared by casting a GO dispersion into a mold and then drying, first at room temperature and then at 60 °C in a vacuum oven overnight. For the thermal treatments, the samples were placed in a tube furnace and heated up in an N_2 atmosphere. The residence time for each temperature was of 60 min.

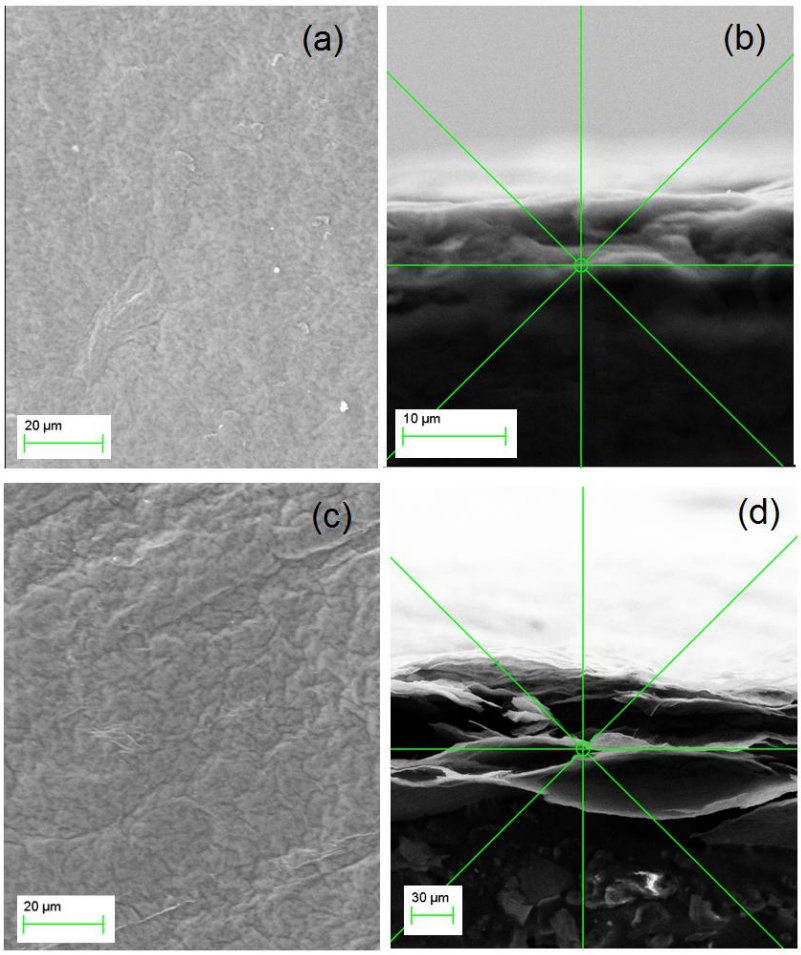

Figure 5-1 Scanning electron microscopy images of the free-standing rGO films. 1a and 1c contain a top view of the films while 1b and 1d provide a cross-sectional view. 1a and 1b demonstrate the reference GO film while 1c and 1d show the rGO film annealed at 600 oC. This data is after J.D. Renteria, S. Ramirez, B. Alonso, A. Zurutuza, H. Malekpour, A.I. Cocemasov, D.L. Nika and A.A. Balandin, Strongly Anisotropic Thermal Conductivity of Free-Standing Reduced Graphene Oxide Films Annealed at High Temperature, Advanced Functional Materials, 25 (2015).

Figure 5-1 shows the top (a–c) and cross-sectional (b–d) scanning electron microscopy (SEM) images of the free-standing films. The representative samples are the reference GO film and rGO film annealed at 600 °C. The cross-sectional SEM images

reveal a layered structure where individual continuous sp^2 layers become larger. The interlayer distance between sp^2 atomic planes does not change substantially after the thermal treatment in line with previous reports that used XRD analysis. [29] At the same time, the "air pockets" develop between the layers as a result of oxygen and carbon dioxide release. The "air pockets" impede strongly the cross-plane thermal transport while not seriously affecting the in-plane thermal conduction. The surface of the high-temperature annealed films becomes corrugated due to the "air pockets" formation and possible contraction. The morphological changes observed in SEM data are corroborated with the thickness data. The average thickness H = 40 μm of the reference GO film increased to H = 170 μm in the rGO film annealed at 1000 °C. The true mass density, ρ_0, measured after compacting the material into the special sample container to avoid the air bubbles was 1.87 g/cm^3 in the reference GO film. It did not change after the high-temperature treatment. The apparent mass density, which includes "air pockets," changed approximately proportionally to the increased thickness.

5.2 Confirmation of Reduction of GO films via XPS and Raman Spectroscopy

The chemical composition and morphology of the samples before and after annealing has been studied using X-ray photoelectron spectroscopy (XPS). All samples exhibited carbon (C), oxygen (O), nitrogen (N), and sulfur (S) at varying concentrations. The XPS spectrum range relevant to the present study is shown in Figure 5-2 a,b. The main peaks

observed at ≈284.6, 286.8, and 288.1 eV correspond to sp^2 and sp^3 C, single-bonded carbon–oxygen (C-O), and double-bonded carbon–oxygen (C=O). Annealing at 600 °C results in a significant reduction of both C-O and C=O bonds followed by an almost complete extinction of such bonds after 1000 °C treatment (see Figure 5-2 a,b). The expulsion of O by thermal treatment leads to the concentration of C exceeding 90 % after 600 °C annealing. The energy difference between C sp^2 and C sp^3 peaks is rather small, which complicates interpretation. However, the reported data for rGO are in agreement that C sp^2 peak energy is in a range 284.1–285 eV while C sp^3 peak energy is in the range 284.9–286 eV. [30–35] The measured peak in rGO film annealed at T = 1000 °C is around 284.8 eV which suggests that it mostly corresponds to C sp^2 bonds. This conclusion is in line with the detailed study of the effects of temperature of reduction of GO. [29]

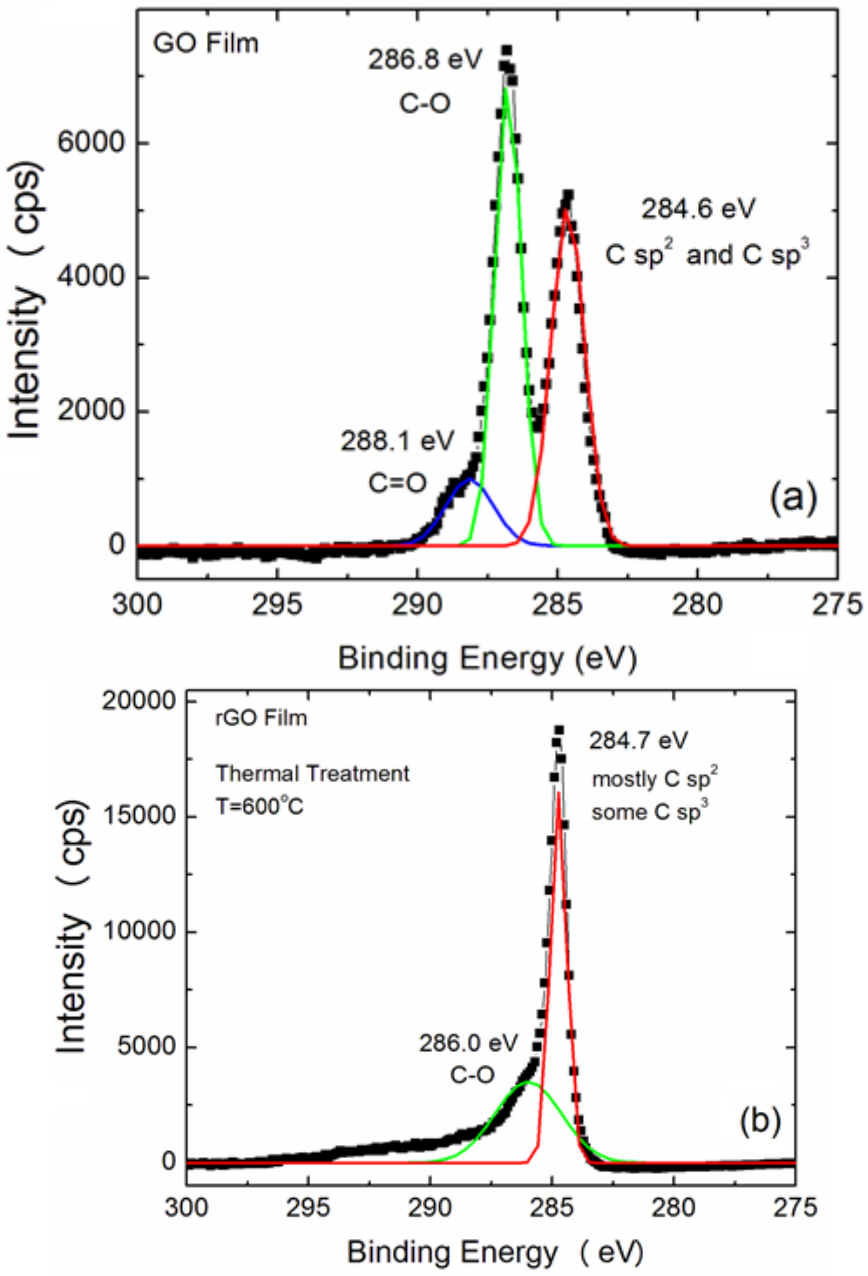

Figure 5-2 X-ray photoelectron spectroscopy data of the carbon signatures for a) reference GO film and b) rGO film thermally treated to 600 °C. The main peaks observed at ≈284.6 (red line), 286.8 (green line), and 288.1 eV (blue line) correspond to sp2 and sp3 C, single-bonded carbon–oxygen (C-O), and double-bonded carbon–oxygen (C=O), respectively. The expulsion of O by thermal treatment leads to the concentration of C exceeding 90 % after 600 °C annealing.

We used Raman spectroscopy as another tool for monitoring how the thermal treatment changes the structural composition of rGO films (see Figure 3 a,b). Raman spectroscopy (Renishaw InVia) was performed in a backscattering configuration under visible (λ = 488 nm) and UV (λ = 325 nm) laser excitations. Details of our Raman experimental procedures have been reported by some of us elsewhere. [36, 37] Figure 3a shows the Raman spectra for rGO samples that underwent thermal treatment at 300, 600, and 1000 ^{o}C. The peaks at $\approx$1350 and 1580 cm^{-1} correspond to the D and G peaks, respectively. The 2D band centered around 2700 cm^{-1} and an S3 peak near 2900 cm^{-1} are also present and consistent with literature reports for rGO. [38–40] It is observed that the separation between the D and G peaks becomes more pronounced with the sample thermally treated at 1000 °C and that the 2D band and S3 peak are also becoming more prominent. These are indications that the GO films underwent reduction as they received thermal treatment and that the films are moving away from an amorphous state to a more ordered material. This is consistent with our XPS data showing that the C-O and C=O bonds have effectively disappeared from the films and help to explain our thermal data. It is known that UV Raman is more sensitive to C sp^3 and C-H bonds. Figure 3 b shows that the I(D)/I(G) intensity ratio decreases substantially in rGO annealed at 1000 °C as compared to that annealed at 300 °C. This suggests that the amount of C sp^3 in the samples treated at 1000 °C is small and the O reduction mostly results in sp^2 bonds, in line with XPS analysis.

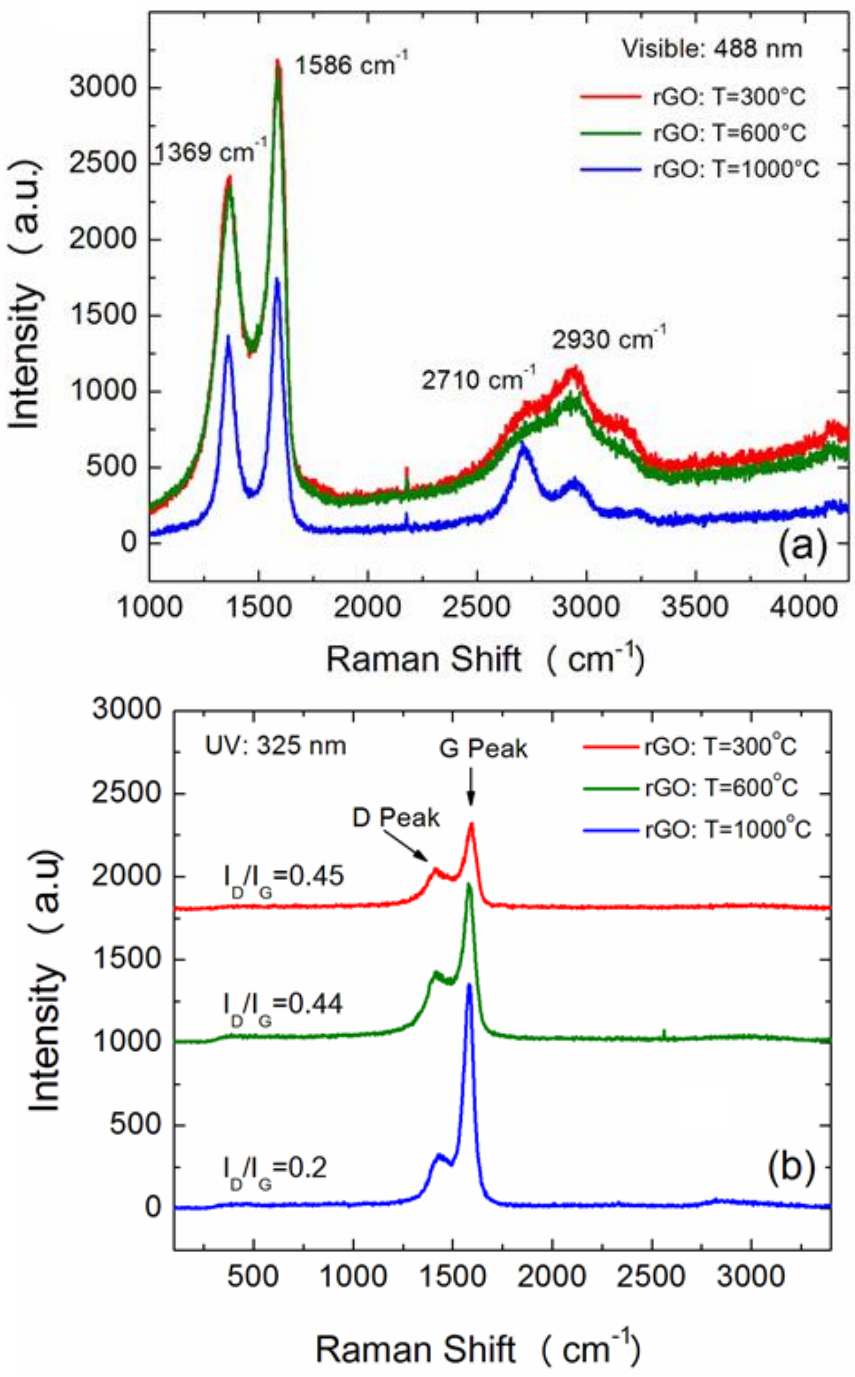
Visible: 488 nm
rGO: T=300°C
rGO: T=600°C
rGO: T=1000°C
1586 cm-1
1369 cm-1
2930 cm-1
2710 cm-1
(a)
Intensity (a.u.)
Raman Shift (cm-1)
UV: 325 nm
G Peak
D Peak
rGO: T=300°C
rGO: T=600°C
rGO: T=1000°C
ID/IG=0.45
ID/IG=0.44
ID/IG=0.2
(b)
Intensity (a.u)
Raman Shift (cm-1)

Figure 5-3 Raman spectra of rGO films under a) visible ($\lambda = 488$ nm) and b) UV ($\lambda = 325$ nm) laser excitations. The Raman spectra are shown a) for rGO samples that underwent thermal treatment at 300, 600, and 1000 °C. The peaks at $\approx$1350 and 1580 cm−1 correspond to the D and G peaks, respectively, which have more pronounced separation with thermal treatment at 1000 °C. The 2D band and S3 peak also become well defined indicating that the films are moving from an amorphous state to a more ordered material. The ratio of the intensity of D peak to that of G peak in Raman spectra under UV excitation b) suggests the reduction in defects and sp3 bonds. This data is after J.D. Renteria, S. Ramirez, B. Alonso, A. Zurutuza, H. Malekpour, A.I. Cocemasov, D.L. Nika and A.A. Balandin, Strongly Anisotropic Thermal Conductivity of Free-Standing Reduced Graphene Oxide Films Annealed at High Temperature, Advanced Functional Materials 25, 4664 (2015).

5.3 Thermal Transport Measurements

The thermal conductivity of the films was studied using the "laser flash" technique (LFT). In addition, the optothermal Raman measurements [8] were performed to cross-check the thermal conductivity values. The LFT transient method directly measures the thermal diffusivity, α, of the material. [41] The thermal conductivity is then determined from the equation $K = \rho\ \alpha\ C_p$, where ρ is the mass density and C_p is the specific heat of the sample. The specific heat is determined from the independent measurement using a calorimeter or a separate measurement with the same apparatus using a reference sample of similar thermal properties with known tabulated C_p (e.g. graphite). The cross-plane α was measured using the "laser flash" method in the standard configuration: the film is heated by light illumination from one side and the temperature rise is measured on the opposite side. The in-plane diffusivity measurement requires a special sample holder where the location for the light input on one side of the sample and location for measuring the temperature increase on the other side of the sample are at different lateral positions. This arrangement ensures that the measured increase of the sample temperature on the back side corresponds to the thermal diffusivity in the in-plane direction [20]. Before performing the measurements with rGO films, we calibrated the experimental system on several known materials.

Figure 5-4 shows the cross-plane component of the thermal conductivity, $K_{\perp}$, as a function of temperature for rGO annealed at different temperatures and a reference GO

film. One notices that $K_{\perp}$ is small for all samples. The most interesting feature is a drastic reduction of $K_{\perp}$ after high-temperature annealing. We explain it by the restoration of the sp^2 bonds within the atomic planes and the action of the "air pockets" (the thermal conductivity of the air is $\approx$0.02 W/mK). The softening of the bonds between the layers may also play a role. Below, we provide a more detailed theoretical analysis to explain this effect. The cross-plane thermal conductivity only weakly depends on temperature revealing a small growth as T increases. The latter is expected for the amorphous and disordered materials. The film thickness non-uniformity and residue defects suggest that in the cross-plane direction the material is rather disordered even after high-temperature treatment. The $K_{\perp}$ value of 0.09 W/mK being extremely small can be considered at the low bound of the amorphous limit [42]. A few cases when thermal conductivity in the cross-plane direction went below the amorphous limit have been reported in the literature [43].

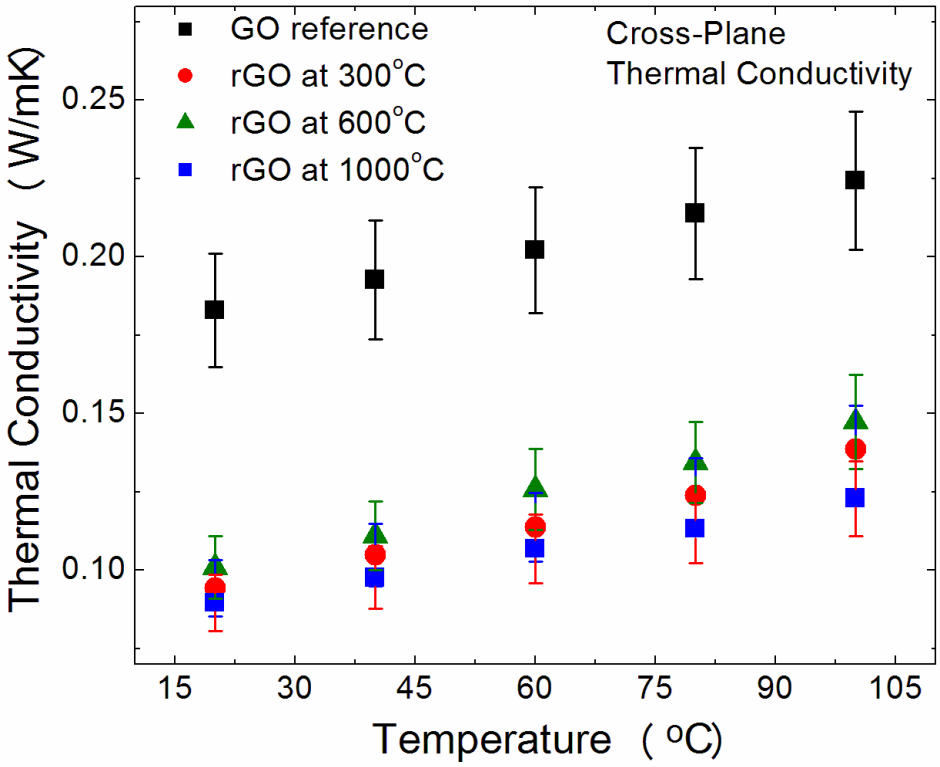

Figure 5-4 Experimental cross-plane thermal conductivity, K⊥, as a function of temperature for rGO annealed at different temperatures and a reference GO film. Note that K⊥ is reduced for high-temperature annealed samples as compared to that of reference GO film. This data is after J.D. Renteria, S. Ramirez, B. Alonso, A. Zurutuza, H. Malekpour, A.I. Cocemasov, D.L. Nika and A.A. Balandin, Strongly Anisotropic Thermal Conductivity of Free-Standing Reduced Graphene Oxide Films Annealed at High Temperature, Advanced Functional Materials 25, 4664 (2015).

The in-plane thermal conductivity, K, is presented as a function of temperature in Figure 5-5. The results are shown for rGO films annealed at 300, 600, and 1000 °C. One can see that the increased temperature of annealing results in higher K values. The room temperature in-plane thermal conductivity increases from 2.9 W/mK for the reference GO film to 61 W/mK for the rGO film annealed at 1000 °C. The rGO films annealed at 300 and 600 °C show increased in-plane thermal conductivity and weak temperature dependence. The slightly increasing K with T for 300 and 600 °C annealed samples

suggests that the phonon thermal transport is still limited by disorder. The thermal conductivity of the rGO film annealed at 1000 °C reveals decreasing K with T indicative of the onset of the Umklapp-scattering limited phonon transport. The rGO films treated at this high temperature start to behave more like crystalline materials although with a very large concentration of defects. In crystalline materials the phonon thermal conductivity decreases as 1/T due to the Umklapp phonon scattering. [8] The increasing K with annealing temperature can be explained by the enlargement of sp^2 grains and reduction in phonon scattering on O and other impurities. This interpretation is supported by the XPS data.

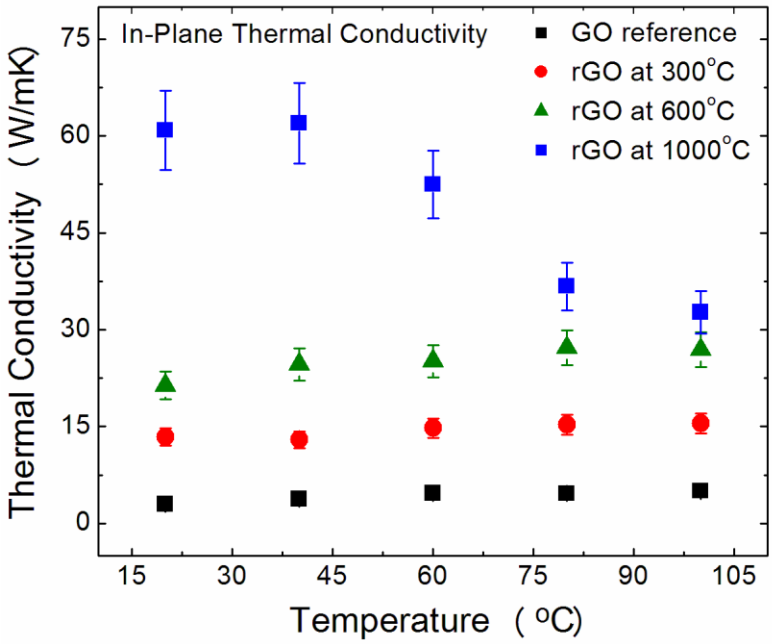

Figure 5-5 Experimental in-plane thermal conductivity, K, as a function of temperature for rGO films annealed at different temperatures and a reference GO film. The higher annealing temperature results in progressively higher K values. The room-temperature thermal conductivity, K, increases from 2.9 W/mK for the reference GO film to 61 W/mK for the rGO film annealed at 1000 °C. This data is after J.D. Renteria, S. Ramirez, B. Alonso, A. Zurutuza, H. Malekpour, A.I. Cocemasov, D.L. Nika and A.A. Balandin, Strongly Anisotropic Thermal Conductivity of Free-Standing Reduced Graphene Oxide Films Annealed at High Temperature, Advanced Functional Materials 25, 4664 (2015).

To cross-check the thermal conductivity values obtained from the "laser flash" technique, we also conducted the optothermal Raman measurements for the 1000 °C annealed films. The optothermal technique was initially developed for the measurement of the thermal conductivity of suspended graphene samples [4–6, 8] and later extended to macroscopic suspended films. [21] The temperature rise in response to the laser heating of the samples was extracted from the G and D peak positions. The experimental details are given in the Supporting Information. The obtained value of the thermal conductivity averaged between G and D peak data was consistent with the "laser flash" data within 7% experimental uncertainty.

5.4 Electrical Resistivity Measurements

It is known that the thermal transport in graphite, graphene and their derivatives is dominated by acoustic phonons. [8, 12] However, it is interesting to compare the changes in the in-plane thermal conductivity with those in electrical conductivity because both the phonon and electron transport can be affected by the defects and structural disorder in carbon materials. We have measured the electrical sheet resistance using the van der Pauw technique. The main finding was that the annealing at high temperature results in the decrease of the resistivity from 0.5 MΩ/□ range to ≈1–19 Ω/□ for the rGO film subjected to annealing at T = 1000 °C. The data for the samples treated at different temperatures are summarized in Table 5T-1, along with data reported previously for rGO

for comparison. The increase of the electrical conductivity of rGO films can be explained by increasing sp^2 phase as in other carbon derivatives. It is also in line with previous studies of electrical conductivity of rGO, which correlated it with the sp^2 (C-C)/sp^3 (C-O, O-C-O) peak ratio in XPS spectra. [34]

Table 5T-1 Comparison of electrical resistivity data for rGO films in this work and literature

Sample + Reduction method	Sheet Resistance (Ω/□)	Reference
GO	0.514 ± 0.236 x 106	This work
rGO (annealed @ T=300 ^{o}C)	27 ± 17	This work
rGO (annealed @ T=600 ^{o}C)	2.01 ± 1.6	This work
rGO (annealed @ T=1000 ^{o}C)	2.13 ± 1.1	This work
Hydrogen and thermal treatment followed	14 x 103	[44]
Hydroiodic acid (HI)	840	[45]
Hydrazine vapor and thermal treatment	100 - 1000	[46]
Thermochemical nanolithography	18 - 9100	[47]
Hydrogen reduction	18	[48]

For our rGO samples, T $\approx$ 1000 ^{o}C can be considered a useful reference annealing temperature at which O reduction and sp^2 bond restoration leads to a drastic increase in K. A detailed study of the effects of temperature on the reduction of GO

found that O reduction and partial exfoliation of graphitic layers starts at temperatures as low as 127 °C. [29] The exfoliation accompanies partial reduction as a consequence of the substantial loss of the oxygen surface groups. When GO is treated at higher temperatures, $T \geqslant 600\ ^{o}C$, the reduction improves, with a loss of O and H and a conversion of hybridized carbon atoms from sp^3 into sp^2 . [29] The authors of ref. [29] also noted that T = 1000 °C appears to be a critical temperature in GO treatment from the point of view of the efficiency of the reduction process, as the resulting graphene-like material contained <2% oxygen and 81.5% C sp^2 . [29] Our findings are in line with this report in terms of the loss of O, increased sp^2 content and enlargement of the graphene-like domains within each layer. All these factors together lead to the observed increase in the in-plane thermal conductivity and unusually high $K / K\perp$ ratio.

5.5 Theoretical Interpretation of Experimental Results

It is interesting to note that despite a significant increase of the thermal conductivity for the thermally treated rGO film (K = 61 W/mK) at RT for rGO annealed at T = 1000 °C), it is still much lower than that in graphite or graphene (K = 2000 W/mK) at RT for basal planes of graphite and can exceed this value in large graphene layers). [8, 12] The reason for this is that the phonon thermal transport in rGO films is still limited not by intrinsic properties of graphene layers but by the grain and disorder scattering. The samples treated at T = 1000 °C only start showing the signs of the intrinsic Umklapp scattering. There have been only a few theoretical computational studies reported for thermal

conductivity of GO and rGO. [49, 50] For this reason, there is a need in the experimentally validated theoretical models that can be used for optimization of the thermal transport in rGO films.

We now turn to theoretical interpretation of the experimental results. For the theoretical investigation of the thermal conductivity in rGO, we adopted our approach, developed for thermal conductivity of graphite in Ref. [11]. In our simulation, we employ graphite phonon energy dispersions, obtained within Born–von Karman model of lattice dynamics, [51, 52] and consider oxygen and other impurities as point defects. Following the approach of Ref. [11], we treat the phonon transport in rGO as 2D for phonons with frequencies $\omega_s > \omega_{c,s}$ and 3D for phonons with $\omega_s \leqslant \omega_{c,s}$, where $\omega_{c,s}$ is the low-bound cutoff frequency of the sth phonon branch. The in-plane thermal conductivity K in-plane is given by

$$K^{in-plane} = K^{3D} + K^{2D}$$

$$K^{3D} \equiv \frac{h^2}{4\pi^2 k_B T^2} \sum_s \int_0^{\omega_{c,s}} q_{z,s}(\omega)\omega^2\tau_s(\omega)v_s^{||}(q_{||}) \frac{\exp\left(\frac{\hbar\omega}{k_B T}\right)}{\left[\exp\left(\frac{\hbar\omega}{k_B T}\right)-1\right]^2} q_{||}\, d\omega \qquad (13)$$

$$K^{2D} \equiv \frac{h^2}{4\pi^2 k_B T^2} \sum_s \frac{\omega_{c,s}}{v_s^{\perp}} \int_{\omega_{c,s}}^{\omega_{max,s}} \omega^2\tau_s(\omega)v_s^{||}(q_{||}) \frac{\exp\left(\frac{\hbar\omega}{k_B T}\right)}{\left[\exp\left(\frac{\hbar\omega}{k_B T}\right)-1\right]^2} q_{||}\, d\omega$$

In Equation (13) $\tau_s(\omega)$ is the relaxation time for a phonon with the frequency ω from the sth acoustic phonon branch, $\mathbf{q}(q_{||}, q_z)$ is the phonon wave vector, $v_s = d\omega/dq^{||}$ is the in-plane phonon group velocity for sth branch, T is the temperature, k_B is the Boltzmann's constant, $\hbar$ is the Planck's constant. The summation in Equation (13) is performed over six lowest phonon branches: in-plane longitudinal acoustic LA_1, in-plane transverse

acoustic TA_1, out-of-plane transverse acoustic ZA, in-plane longitudinal acoustic-like LA_2, in-plane transverse acoustic-like TA_2, and out-of-plane transverse acoustic-like ZO'.

We assume that the Umklapp scattering (*U*), point-defect scattering (*PD*) and scattering on ordered clusters edges (*E*) are the main mechanisms limiting the thermal conductivity in rGO. The total phonon relaxation time τ was calculated using the Matthiessen's rule as [11-12, 3, 53-55]: $1/\tau_s = 1/\tau_{PD,s} + 1/\tau_{U,s} + 1/\tau_{E,s}$, where $\tau_{U,s}(\omega) = Mv_s^2\omega_{\max,s}/(\gamma_s^2 k_B T[\omega]^2)$, $\tau_E(\omega) = L/v_s^{\|}$ and $\tau_{PD,s}(\omega) = 4v_s^{\|}/(S_0\Gamma q^{\|}\omega^2)$. Here $\gamma_{LA_1,LA_2} = 2$, $\gamma_{TA_1,TA_2} = 1$ and $\gamma_{ZA,ZO'} = -1.5$ is the branch-dependent average Gruneisen parameters, $\omega_{\max,s}$ is the maximum frequency of *s*-th phonon branch, S_0 is the cross-section area per atom, *M* is the graphite unit cell mass, Γ is the measure of the strength of the point-defect scattering due to mass-difference and *L* is the average length of ordered sp^2 or sp^3 clusters. The values of $\omega_{c,s}$ were determined from the phonon spectra as the highest energy of *s*-th branch along c-axis direction: $\omega_{c,LA_1/LA_2} = 89$ cm^{-1}, $\omega_{c,TA_1/TA_2} = 89$ cm^{-1} and $\omega_{c,ZA/ZO'} = 32\,cm^{-1}$. The strength of the point-defect scattering Γ was estimated from the following formula [3]: $\Gamma = \sum_i c_i(\Delta M_i/M_C)^2$, where $\Delta M_i = M_{d,i} - M_C$ is the difference between mass of the point-defect $M_{d,i}$ and carbon mass M_C, c_i is the ratio between the concentrations of the defects *i* and carbon atoms. We consider an impurity atom attached to a carbon atom as a point-defect in the graphite lattice. Our XPS study revealed that the three main impurity atoms present in our samples are O, N, and S. The Γ

parameter was calculated for each sample separately taking into account actual concentrations of defects. The defect concentrations and obtained values of Γ are listed in Table 5T-2.

Figure 5T-2 Elemental composition and Γ parameter values.

	C (%)	O (%)	S (%)	N (%)	Γ
GO	65.9	29.2	3.7	1.1	1.208
rGO(T=300^{o}C)	89.4	10.3	0.3	0	0.229
rGO(T=600^{o}C)	90.6	8.6	0.4	0.4	0.206
rGO(T=1000^{o}C)	91.9	6.7	1	0.4	0.213

The dependence of the in-plane thermal conductivity, calculated from Eq. (1) is shown in Figure 6 (a) as a function of the average length L of the ordered graphitic clusters. The results are presented for different values of Γ. The thermal treatment enhances the thermal conductivity of rGO due to the following reasons: (i) decrease of the defect concentrations, (ii) increase of the lateral dimensions of the ordered clusters and (iii) the rise of the sp^2 fraction. The oxygen concentration permanently decreases with temperature in our samples (see Table 5T-2). Nevertheless, the parameter $\Gamma \sim 0.21$ is estimated for all thermally treated rGO due to difference in S and N content. It means that the point-defect scattering is roughly the same for all treated rGO and by a factor of six weaker than in GO. The latter allows one to make a conclusion that increasing of the lateral dimensions of the ordered clusters is the key reason for the thermal conductivity enhancement in rGO samples. The restoring of the highly ordered graphene-like lattice after treatment was reported in Refs. [29, 34-35]. Comparing the theoretical and

experimental thermal conductivity data we can roughly estimate the average length of the ordered clusters: it increases from ~ 3.5 nm in GO to ~ 500 nm in rGO (T=1000^{o}C). The obtained L ~ 500 nm are in range of the average grain lengths 250 nm – 30 μm reported for polycrystalline graphene [56] and graphite [57]. The actual average cluster length in our rGO samples could be even larger due to possible additional phonon scattering on vacancies and dislocations. The vacancy concentration ~ 0.5% increases theoretical L up to 800 nm for rGO (T=1000^{o}C). The increase of L in rGO accelerates with temperature: in rGO (T=600^{o}C) the L value is by a factor of three larger than in rGO (T=300^{o}C) while in rGO (T=1000^{o}C) it increases by a factor of 16 as compared with rGO (T=600^{o}C). The thermal conductivity of rGO can be increased up to ~ 500 W/mK for samples with larger grains and reduced impurities. In Figure 6 (b) we illustrate the impact of the oxygen reduction on the thermal conductivity of rGO. For this plot we assumed that only oxygen impurities are present in rGO. Decreasing O concentration from 50% to 1% increases K by a factor of 4 – 24 depending on the average cluster size L. Our calculations show that S and N impurities in rGO (T=1000^{o}C) suppress K by 28%. Removing these impurities together with reducing O concentration down to 1% allows to obtain K ~ 300 W/mK at L ~ 500 nm.

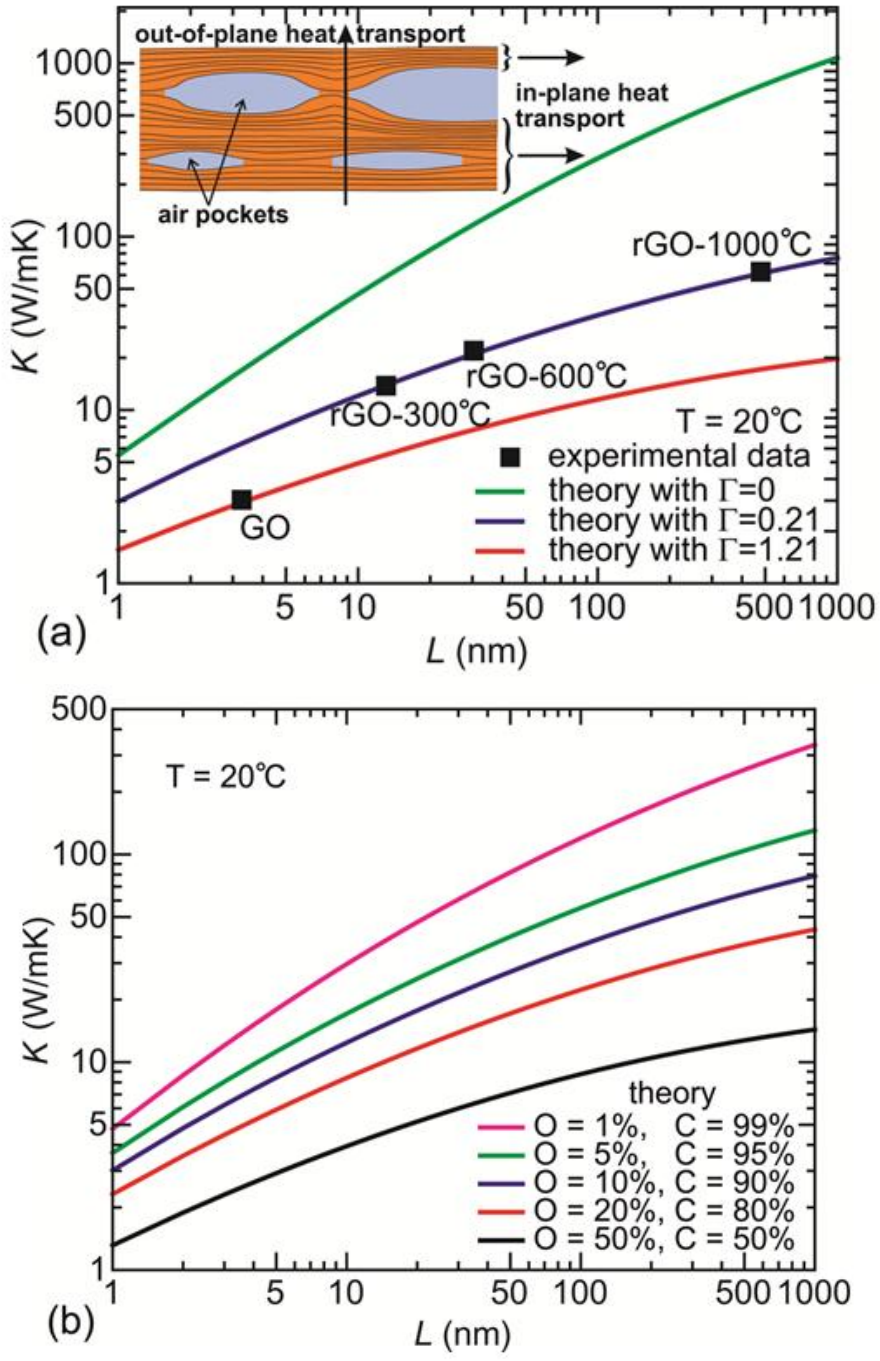

Figure 5-6 Calculated in-plane thermal conductivity of GO and rGO at T = 20 °C as a function of the average cluster size L. The data provide a) comparison between the theoretical calculations and experimental data and b) illustrate the effect of the oxygen impurity. This data is after J.D. Renteria, S. Ramirez, B. Alonso, A. Zurutuza, H. Malekpour, A.I. Cocemasov, D.L. Nika and A.A. Balandin, Strongly Anisotropic Thermal Conductivity of Free-Standing Reduced Graphene Oxide Films Annealed at High Temperature, Advanced Functional Materials 25, 4664 (2015).

The decrease of the cross-of-plane thermal conductivity in rGO with the higher treatment temperature can be qualitatively explained by an increase in the number and size of the "air pockets" between rGO multilayers (see inset to Figure 6 (a) and Figures 1 (b-d)). The average thickness of rGO film treated at 1000^0C is by a factor of four larger than that of the GO film indicating the increase in the "air pocket" volume. The cross-plane thermal transport is affected by the "air pockets" much more than the in-plane thermal transport. In the Maxwell-Garnett's effective medium approximation, the cross-plane thermal conductivity can be estimated as [58]:

$$K_{rGO}^{\perp}(\varphi) = K_{GO}^{\perp} \frac{(1-\varphi)(K_{air} + 2K_{GO}^{\perp}) + 3\varphi K_{air}}{(1-\varphi)(K_{air} + 2K_{GO}^{\perp}) + 3\varphi K_{GO}^{\perp}}, \quad (14)$$

where φ is the volume fraction of the "air pockets", $K_{GO}^{\perp}$ is the thermal conductivity of the non-treated GO and K_{air} is the thermal conductivity of air. Using $K_{GO}^{\perp} \approx 0.18\,\mathrm{W/mK}$, $K_{air} \approx 0.026\,\mathrm{W/mK}$, and $\varphi \sim 0.5-0.6$ we obtained $K_{rGO}^{\perp}$ ~0.075-0.09 W/mK, which is in a good agreement with the experimental value of 0.09±0.01 W/mK for rGO (T=1000 ^{o}C) at T = 20 ^{o}C. A theoretical analysis of the dependence of thermal conductivity on the concentration and shape of the "air pockets" is reserved for future study. One should note that formation of the "air pockets" with corresponding reduction in the apparent mass density happens at annealing high temperature. The thermal cycling in the temperature range between RT and 100 ^{o}C above RT, which is characteristic for electronic devices, does not result in additional "air pockets" and layer separation.

5.6 Discussion

In conclusions, we investigated the thermal conductivity of free-standing rGO films subjected to a high-temperature treatment T=300^{o}C, 600^{o}C and 1000°C. It was found that the high-temperature treatment dramatically increased the room-temperature in-plane thermal conductivity, K, from 2.94 W/mK in the reference GO film to 61.8 W/mK in the rGO film annealed at T=1000^{o}C. The cross-plane thermal conductivity, $K_{\perp}$, revealed an intriguing opposite trend of decreasing from ~0.18 W/mK in the reference GO film to ~0.09 W/mK in the rGO film annealed at T=1000^{o}C. The obtained films demonstrated an exceptionally strong anisotropy of the thermal conductivity, $K/K_{\perp}$ ~ 675, which is substantially larger even than in the high-quality graphite ($K/K_{\perp}$~100). The electrical resistivity of the annealed films reduced from a 0.5MΩ/□ range in the reference GO film to 1 Ω/□ – 19 Ω/□ in the high-temperature treated rGO films. The observed modifications of the in-plane and cross-plane thermal conductivity components resulting have been explained theoretically. The increase of the in-plane thermal conductivity is due to restoration of C sp^2 bonds, decreased phonon scattering on O and other impurities and increase in the sp^2 grains. The decrease of the cross-plane thermal conductivity after high-temperature annealing is due to appearance of "air pockets" and softening of the restoring forces in this direction. The strongly anisotropic heat conduction properties of rGO films treated at high temperature can be useful for applications in thermal management, which requires materials which can remove excess heat (high K) along one direction and shield from heat (lower $K_{\perp}$) along the perpendicular direction.

5.7 Summary

In this Chapter, we demonstrated that annealing GO films results in rGO films with highly anisotropic thermal transport. We have demonstrated that C-O and C=O bonds almost disappear when GO films are annealed at higher temperatures, with the critical annealing temperature at T = 1000 ^{o}C. Not only that, we observed thermal conductivity for cross-plane decreases greatly, as low as 0.09 W/mK after reduction, however, in-plane thermal conductivity increases greatly, up to 61 W/mK after reduction. We also demonstrated that reduction by annealing leads to a very great decrease in electrical resistivity, the lowest reported to date. These results are important for thermal management of electronics where very highly anisotropic heat transport, $K/K_{\perp}$, is needed and could be also used as a thermally conductivity filler material in preparation of composites, specifically, magnetic composites.

References

[1] R. Prasher, *Proc.,"Thermal Interface Materials: Historical Perspective, Status, and Future Directions,"* IEEE **94**, 1571 (2006).

[2] C. Y. Ho, R. W. Powell and P. E. Liley, *"Thermal Conductivity of the Elements: A Comprehensive Review."* J. Phys. Chem. Ref. Data **3**, 1 (1974)

[3] P. G. Klemens and D. F. Pedraza, *"Thermal Conductivity of Graphite in the Basal Plane,"* Carbon **32**, 735 (1994)

[4] A. A. Balandin, S. Ghosh, W. Bao, I. Calizo, D. Teweldebrhan, F. Miao and C. N. Lau, *"Superior Thermal Conductivity of Single-Layer Graphene,"* Nano Lett. **8**, 902 (2008)

[5] S. Ghosh, W. Bao, D. L. Nika, S. Subrina, E. P. Pokatilov, C. N. Lau and A. A. Balandin, *"Dimensional Crossover of Thermal Transport in Few-Layer Graphene,"* Nat. Mater. **9**, 555 (2010)

[6] W. Cai, A. L. Moore, Y. Zhu, X. Li, S. Chen, L. Shi and R. Ruoff, *"Thermal Transport in Suspended and Supported Monolayer Graphene Grown by Chemical Vapor Deposition,"* Nano Lett. **10**, 1645 (2010)

[7] J. H. Seol, I. Jo, A. L. Moore, L. Lindsay, Z. H. Aitken, M. T. Pettes, X. Li, Z. Yao, R. Huang, D. Broido, N. Mingo, R. S. Ruoff and L. Shi, *"Two-Dimensional Phonon Transport in Supported Graphene,"* Science **328**, 213 (2010)

[8] A. A. Balandin, *"Thermal Properties of Graphene and Nanostructured Carbon Materials,"*Nat. Mater. **10**, 569 (2011)

[9] D. L. Nika, E. P. Pokatilov, A. S. Askerov and A. A. Balandin, *"Phonon Thermal Conduction in Graphene: Role of Umklapp and Edge Roughness Scattering,"* Phys. Rev. B **79**, 155413 (2009)

[10] L. Lindsay, D. A. Broido and N. Mingo, *"Diameter Dependence of Carbon Nanotube Thermal Conductivity and Extension to the Graphene Limit,"* Phys. Rev. B **82**, 161402 (2010)

[11] D. L. Nika, A. S. Askerov and A. A. Balandin, *"Anomalous Size Dependence of the Thermal Conductivity of Graphene Ribbons,"* Nano Lett. **12**, 3238 (2012)

[12] D. L. Nika and A. A. Balandin,"*Two-Dimensional Phonon Transport in Graphene,"* J. Phys.: Condens. Matter **24**, 233302 (2012)

[13] S. Mei, L. N. Maurer, Z. Aksamija and I. Knezevic, *"Full-Dispersion Monte Carlo Simulation of Phonon Transport in Micron-Sized Graphene Nanoribbons,"* J. Appl. Phys. **116**, 164307 (2014)

[14] G. Fugallo, A. Cepellotti, L. Paulatto, M. Lazzeri, N. Marzari and F. Mauri, *"Thermal Conductivity of Graphene and Graphite: Collective Excitations and Mean Free Paths,"* Nano Lett. **14**, 6109 (2014)

[15] K. M. F. Shahil and A. A. Balandin, *"Graphene–Multilayer Graphene Nanocomposites as Highly Efficient Thermal Interface Materials,"* Nano Lett. **12**, 861 (2012)

[16] J. D. Renteria, D. L. Nika and A. A. Balandin, *"Graphene Thermal Properties: Applications in Thermal Management and Energy Storage,"* Appl. Sci. **4**, 525 (2014)

[17] Z. Yan, D. L. Nika and A. A. Balandin, *"Thermal Properties of Graphene and Few-Layer Graphene: Applications in Electronics,"* IET Circuits, Devices & Systems **9**, 4 (2015)

[18] Z. Yan, G. Liu, J. M. Khan and A. A. Balandin, *"Graphene Quilts for Thermal Management of High-Power GaN Transistors,"*Nat. Commun. **3**, 827 (2012)

[19] S.-H. Bae, R. Shabani, J.-B. Lee, S.-J. Baeck, H. J. Cho and J.-H Ahn, *"Graphene-Based Heat Spreader for Flexible Electronic Devices,"* IEEE Trans. Electron Devices **61**, 4171 (2014)

[20] P. Goli, H. Ning, X. Li, C. Y. Lu, K. S. Novoselov and A. A. Balandin, *"Thermal Properties of Graphene–Copper–Graphene Heterogeneous Films,"* Nano Lett. **14**, 1497 (2014)

[21] H. Malekpour, K.-H. Chang, J.-C. Chen, C. Y. Lu, D. L. Nika, K. S. Novoselov and A. A. Balandin, *"Thermal Conductivity of Graphene Laminate,"* Nano Lett. **14**, 5155 (2014)

[22] W. S. Hummers and R. E. Offeman, *"Preparation of Graphitic Oxide,"* J. Am. Chem. Soc. **80**, 1339 (1958)

[23] C. Gómez-Navarro, R. T. Weitz, A. M. Bittner, M. Scolari, A. Mews, M. Burghard and K. Kern, *"Electronic Transport Properties of Individual Chemically Reduced Graphene Oxide Sheets,"* Nano Lett. **7**, 3499 (2007)

[24] D. A. Dikin, S. Stankovich, E. J. Zimney, R. D. Piner, G. H. Dommett, G. Evmenenko, S. T. Nguyen and R. S. Ruoff, *"Preparation and Characterization of Graphene Oxide Paper,"*Nature **448**, 457 (2007)

[25] C. Chen, Q.-H. Yang, Y. Yang, W. Lv, Y. Wen, P.-X. Hou, M. Wang and H.-M. Cheng, *"Self-Assembled Free-Standing Graphite Oxide Membrane,"* Adv. Mater. **21**, 3007 (2009)

[26] Y. Zhu, S. Murali, W. Cai, X. Li, J. W. Suk, J. R. Potts and R. S. Ruoff, *"Graphene and Graphene Oxide: Synthesis, Properties, and Applications,"* Adv. Mater. **22**, 3052 (2010)

[27] L. Tian, P. Anilkumar, L. Cao, C. Y. Kong, M. J. Meziani, H. Qian, L. M. Veca, T. J. Thorne, K. N. Tackett II, T. Edwards and Y.-P. Sun, *"Graphene Oxides Dispersing*

and Hosting Graphene Sheets for Unique Nanocomposite Materials," ACS Nano **5**, 3052 (2011)

[28] C. Y. Kong, W.-L. Song, M. J. Meziani, K. N. Tackett II, L. Cao, A. J. Farr, A. Anderson and Y.-P. Sun, *"Supercritical Fluid Conversion of Graphene Oxides,"* J. Supercrit. Fluids **61**, 206 (2012)

[29] C. Botas, P. Álvarez, C. Blanco, R. Santamaría, M. Granda, M. D. Gutiérrez, F. Rodríguez-Reinoso and R. Menéndez, *"Critical Temperatures in the Synthesis of Graphene-Like Materials by Thermal Exfoliation-Reduction of Graphite Oxide,"* Carbon **52**, 476 (2013)

[30] K. H. Kim, M. Yang, K. M. Cho, Y.-S. Jun, S. B. Lee and H.-T. Jung, *"High Quality Reduced Graphene Oxide through Repairing with Multi-Layered Graphene Ball Nanostructures,"* Sci. Rep. **3**, 3251 (2013)

[31] C.-H. Chuang, Y.-F. Wang, Y.-C. Shao, Y.-C. Yeh, D.-Y. Wang, C.-W. Chen, J. W. Chiou, S. C. Ray, W. F. Pong, L. Zhang, J. F. Zhu and J. H. Guo, *"The Effect of Thermal Reduction on the Photoluminescence and Electronic Structures of Graphene Oxides,"* Sci. Rep. **4**, 4525 (2014)

[32] M. Boutchich, A. Jaffré, D. Alamarguy, J. Alvarez, A. Barras, Y. Tanizawa, R. Tero, H. Okada, T. V. Thu, J. P Kleider and A. Sandhu, *"Characterization of Graphene Oxide Reduced Through Chemical and Biological Processes,"* J. Phys.: Conf. Ser. **433**, 012001 (2013)

[33] A. R. Barron and A. Bratt, "*XPS of Carbon Nanomaterials,"* Openstax CNX. http://cnx.org/content/m34549/1.2/ (accessed Mar 16, 2015).

[34] M. Singh, A. Yadav, S. Kumar and P. Agarwal, *"Annealing Induced Electrical Conduction and Band Gap Variation in Thermally Reduced Graphene Oxide Films with Different sp 2/sp 3 Fraction,"*Appl. Surf. Sci. **326**, 236 (2015)

[35] X. Díez-Betriu, S. Álvarez-García, C. Botas, P. Álvarez, J. Sánchez-Marcos, C. Prieto, R. Menéndez and A. de Andrés, *"Raman Spectroscopy for the Study of Reduction Mechanisms and Optimization of Conductivity in Graphene Oxide Thin Films,"* J. Mater. Chem. C **1**, 6905 (2013)

[36] I. Calizo, A. A. Balandin, W. Bao, F. Miao and C. N. Lau, *"Temperature Dependence of the Raman Spectra of Graphene and Graphene Multilayers," Nano Lett*. **7**, 2645 (2007)

[37] I. Calizo, I. Bejenari, M. Rahman, G. Liu and A. A. Balandin, *"Ultraviolet Raman Spectroscopy of Single and Multi-Layer Graphene,"* J. Appl. Phys. **106**, 043509 (2009)

[38] Y. Zhou, Q. Bao, B. Varghese, L. A. L. Tang, C. K. Tan, C.-H. Sow and K. P. Loh, *"Microstructuring of Graphene Oxide Nanosheets Using Direct Laser Writing,"* Adv. Mater. **22**, 67 (2010)

[39] D. Yang, A. Velamakanni, G. Bozoklu, S. Park, M. Stoller, R. D. Piner, S. Stankovich, I. Jung, D. A. Field, C. A. Ventrice Jr. and R. S. Ruoff, *"Chemical Analysis of Graphene Oxide Films After Heat and Chemical Treatments by X-Ray Photoelectron and Micro-Raman Spectroscopy,"* Carbon **47**, 145 (2009)

[40] T. V. Cuong, V. H. Pham, Q. T. Tran, S. H. Hahn, J. S. Chung, E. W. Shin and E. J. Kim, *"Photoluminescence and Raman Studies of Graphene Thin Films Prepared by Reduction of Graphene Oxide,"* Mater. Lett. **64**, 399 (2010)

[41] W. J. Parker, R. J. Jenkins, C. P. Butler and G. L. Abbot, *"Flash Method of Determining Thermal Diffusivity, Heat Capacity, and Thermal Conductivity,"* J. Appl. Phys. **32**, 1679 (1961)

[42] D. G. Cahill, S. K. Watson and R.O. Pohl, *"Lower Limit to the Thermal Conductivity of Disordered Crystals,"* Phys. Rev. B **46**, 6131 (1992)

[43] C. Chiritescu, D. G. Cahill, N. Nguyen, D. Johnson, A. Bodapati, P. Keblinski and P. Zschack, *"Ultralow Thermal Conductivity in Disordered, Layered WSe2 Crystals,"* Science **315**, 351 (2007)

[44] V. López, R.S. Sundaram, C. Gómez‐Navarro, D. Olea, M. Burghard, J. Gómez-Herrero, F. Zamora and K. Kern, *"Chemical Vapor Deposition Repair of Graphene Oxide: A Route to Highly‐Conductive Graphene Monolayers,"* Adv. Mater. **21**, 4683 (2009)

[45] S. Pei, J. Zhao, J. Du, W. Ren and H. M. Cheng, *"Direct Reduction of Graphene Oxide Films into Highly Conductive and Flexible Graphene Films by Hydrohalic Acids,"* Carbon **48**, 4466 (2010)

[46] H. A. Becerril, J. Mao, Z. Liu, R. M. Stoltenberg, Z. Bao and Y. Chen, *"Evaluation of Solution-Processed Reduced Graphene Oxide Films as Transparent Conductors,"* ACS Nano **2**, 463 (2008)

[47] Z. Wei, D. Wang, S. Kim, S.-Y. Kim, Y. Hu, M. K. Yakes, AR Laracuente, Z Dai, SR Marder, C Berger, WP King, W. A. de Heer, P. E. Sheehan and E. Riedo, *"Nanoscale Tunable Reduction of Graphene Oxide for Graphene Electronics,"* Science **328**, 1373 (2010)

[48] T. Qiu, B. Luo, M. Liang, J. Ning, B. Wang, X. Li and L. Zhi, *"Hydrogen Reduced Graphene Oxide/Metal Grid Hybrid Film: Towards High Performance Transparent Conductive Electrode for Flexible Electrochromic Devices,"* Carbon **81**, 232 **(**2014)

[49] S. Lin and M. J. Buehler,*" Thermal Transport in Monolayer Graphene Oxide: Atomistic Insights into Phonon Engineering Through Surface Chemistry,"* Carbon **77**, 351 (2014)

[50] X. Mu, X. Wu, T. Zhang, D. B. Go and T. Luo, *"Thermal Transport in Graphene Oxide–From Ballistic Extreme to Amorphous Limit,"* Sci. Rep. **4**, 3909 (2014)

[51] A. I. Cocemasov, D. L. Nika and A. A. Balandin, *"Phonons in Twisted Bilayer Graphene,"* Phys. Rev. B **88**, 035428 (2013)

[52] D. L. Nika, A. I. Cocemasov and A. A. Balandin, *"Specific Heat of Twisted Bilayer Graphene: Engineering Phonons by Atomic Plane Rotations,"* Appl. Phys. Lett. **105**, 031904 (2014)

[53] P. G. Klemens, *"Theory of the a-Plane Thermal Conductivity of Graphite,"* J. Wide Bandgap Mater. **7**, 332 (2000)

[54] D. L. Nika, S. Ghosh, E. P. Pokatilov and A. A. Balandin, *"Lattice Thermal Conductivity of Graphene Flakes: Comparison with Bulk Graphite,"* Appl. Phys. Lett. **94**, 2030103 (2009)

[55] Z. Aksamija and I. Knezevic, *"Lattice Thermal Conductivity of Graphene Nanoribbons: Anisotropy and Edge Roughness Scattering,"* Appl. Phys. Lett. **98**, 141919 (2011)

[56] P. Y. Huang, C. S. Ruiz-Vargas, A. M. van der Zande, W. S. Whitney, M. P. Levendorf, J. W. Kevek, S. Garg, J. S. Alden, C. J. Hustedt, Y. Zhu, J. Park, P. L. McEuen and D. A. Muller, *"Grains and Grain Boundaries in Single-Layer Graphene Atomic Patchwork Quilts,"* Nature **469**, 389 **(**2011)

[57] S. Y. Park, H. C. Floresca, Y. J. Suh and M. J. Kim, *"Electron Microscopy Analyses of Natural and Highly Oriented Pyrolytic Graphites and the Mechanically Exfoliated Graphenes Produced From Them,"* Carbon **48**, 797 **(**2010)

[58] C. Pang, J. Y. Jung, J. W. Lee and Y. T. Kang, *"Thermal Conductivity Measurement of Methanol-Based Nanofluids with Al_2O_3 and SiO_2 Nanoparticles,"* U.S. Internat. Jour. of Micro-Nano Scale Transp. **4**, 269 **(**2010)

[59] G. Eda, G. Fanchini and M. Chhowalla, *"Large-Area Ultrathin Films of Reduced Graphene Oxide as a Transparent and Flexible Electronic Material,"* Nat. Nanotechnol. **3**, 270 **(**2008)

[60] M. Hirata, T. Gotou, S. Horiuchi, M. Fujiwara and M. Ohba, *"Thin-Film Particles of Graphite Oxide 1:: High-Yield Synthesis and Flexibility of the Particles,"* Carbon **42**, 2929 **(**2004)

[61] S. Stankovich, D. A. Dikin, R. D. Piner, K. A. Kohlhaas, A. Kleinhammes, Y. Jia, Y. Wu, S. T. Nguyen and R. S. Ruoff, *"Synthesis of Graphene-Based Nanosheets via Chemical Reduction of Exfoliated Graphite Oxide,"* Carbon **45**, 1558 **(**2007)

[62] R. Ikkawi, N. Amos, A. Lavrenov, A. Krichevsky, D. Teweldebrhan, S. Ghosh, A. A. Balandin, D. Litvinov and S. Khizroev, *","Near-Field Optical Transducer for Heat-Assisted Magnetic Recording for Beyond-10-Tbit/in2 Densities"* J. Nanoelectron. Optoelectron. **3**, 44 **(**2008)

[63] S. Ghosh, D. Teweldebrhan, J. R. Morales, J. E. Garay and A. A. Balandin, *"Thermal Properties of the Optically Transparent Pore-Free Nanostructured Yttria-Stabilized Zirconia,"* J. Appl. Phys. **106**, 113507 **(**2009)

Chapter 6

Concluding Remarks

We described in this dissertation the results of our study of the thermal properties of three groups of nanostructured materials: (i) magnetic; (ii) reduced graphene oxide films; and (iii) hybrid magnetic – graphite – graphene composites. Although the investigated materials are distinctively different there are similarities in mechanisms limiting heat conduction in synergy in applications of our thermal conductivity results. The data reported in this dissertation suggest that graphene, graphite and reduced graphene oxide fillers can be used as thermal fillers in nanostructured magnetic materials.

The thermal measurements reported in this dissertation were conducted using the transient "hot disk" and "laser flash" techniques. The used methods allowed us to study in-plane and cross-plane heat conduction thus revealing its anisotropic nature. The rare-earth free nanostructured $SrFe_{12}O_{19}$ permanent magnets were produced by the current activated pressure assisted densification technique. The thermal conductivity of the nanostructured bulk magnets was found to range from 3.8 to 5.6 W/mK for the in-plane and 2.36 W/mk to 2.65 W/mK for the cross-plane directions, respectively. The heat conduction was dominated by phonons near the room temperature. The anisotropy of heat conduction was explained by the brick-like alignment of crystalline grains with the longer grain size in-plane direction. The thermal conductivity scales up with the average grain size and mass density of the material revealing weak temperature dependence.

The proposed concept of graphene – graphite thermal fillers was verified using the nanostructured ferromagnetic Fe_3O_4 composites as an example system. We incorporated graphene and graphite fillers into magnetic material without changing their morphology. It was demonstrated that addition of 5 wt. % of equal mixture of graphene and graphite fillers to the composite results in a factor of ×2.6 enhancement of the thermal conductivity without significant degradation of the saturation magnetization.

In the framework of this dissertation research we investigated the thermal conductivity of free-standing reduced graphene oxide films subjected to a high-temperature treatment of up to 1000°C. It was found that the high-temperature annealing dramatically increased the in-plane thermal conductivity, K, of the films from ~3 W/mK to ~61 W/mK at room temperature. The cross-plane thermal conductivity, $K_{\perp}$, revealed an interesting opposite trend of decreasing to a very small value of ~0.09 W/mK in the reduced graphene oxide films annealed at 1000^{o}C. The obtained films demonstrated an exceptionally strong anisotropy of the thermal conductivity, $K/K_{\perp}$ ~ 675, which is substantially larger even than in the high-quality graphite. The strongly anisotropic heat conduction properties of these films can be useful for the thermal filler applications. The results obtained for the nanostructured magnetic and hybrid materials are important for the renewable energy and electronic applications of permanent magnets.